Tampere University

Elina Anttola

FRONT CONTACT OPTIMIZATION FOR CONCENTRATOR III–V SEMICONDUCTOR SOLAR CELLS

ABSTRACT

Elina Anttola: Front contact optimization for concentrator III−V semiconductor solar cells
Master's thesis
Tampere University
Engineering and Natural Sciences
June 2021

Photovoltaic energy systems are a promising technology for reducing the need of fossil fuels. To date, the highest efficiencies have been reached with multijunction solar cells fabricated from III–V semiconductor compounds. These devices utilize the solar spectrum effectively by dividing it into separate semiconductor layers with specified band gap energies. Compared to single-junction solar cells, the multijunction structure produces less optical and thermal losses. The world-record efficiency has been reached with a multijunction solar cell illuminated with concentrated sunlight. When sunlight is concentrated with optical elements, such as lenses and mirrors, the area of the solar cell can be significantly reduced, which results in considerable material and cost savings. When the intensity of the incident sunlight is multiplied according to the concentration factor, the amount of current produced in a solar cell increases.

When the increased current flows through the semiconductor layers and through the metal contacts of the solar cell into the external load, power losses are produced. One way to compensate the power losses is by optimizing the front contact grid design. In general, the balance must be found between the resistive losses and the shadowing effect associated with the front contact. This thesis work was focused on the optimization of the linear front contact design through literature and experimental research. In the experiments, III-V semiconductor solar cells were fabricated with different contact finger spacings varying from 20 µm to 125 µm. The solar cell structures were grown by molecular beam epitaxy, and photolithographic processing in the cleanroom environment was used to prepare the solar cell devices. The fabrication of the solar cell devices was successful and reliable characterization was possible. The electrical characterization of the solar cells was focused on the top cell of a multijunction solar cell since it acts as a lateral current-spreading layer, and therefore, it can be assumed that the front contact has the most effect on the electrical behaviour of the top cell. The current-voltage behaviour of the solar cells was measured under one-sun and concentrated conditions, which showed predicted behaviour. The highest measured efficiency had the value of 13.48% with the contact finger spacing of 75 µm under the concentration level of 200×. Moreover, the electrical behaviour of the solar cells was significantly affected by increasing the concentration level from 200× to 1000× which showed the domination of resistive losses over the shadowing with the wider contact finger spacings. When the concentration factor was increased to 1000, it was observed that the optimal finger spacing giving the highest efficiency was reduced to 40 µm.

For the further optimization of the properties of the front contact, a simulation model based on Mathworks Simulink-tool was developed allowing the simulations of the current-voltage behaviour of the solar cells under varying concentrated conditions. Based on the simulated results, it was shown that the good conductivity of metal becomes significant when the dimensions of the contact fingers are reduced. Therefore, the further investigation of silver-based front contacts should be considered. The dimensions of the front contact in the simulations were chosen based on the limitations set by the photolithographic fabrication technique.

Based on the study conducted in this thesis work, optimized finger spacing, and the design of the front contact grid was experimentally achieved for the solar cells in concentrator use. Furthermore, these results are essential in the research on the multijunction solar cells reaching ultra-high efficiencies over 50%.

Keywords: front contact grid, multijunction solar cell, III–V semiconductor, concentrated photovoltaics, current-voltage, characterization

TIIVISTELMÄ

Aurinkoenergian yhä tehokkaampi hyödyntäminen on välttämätöntä fossiilisten polttoaineiden korvaamisella uusiutuvilla energialähteillä. Tällä hetkellä tehokkaimmat ja korkeimman hyötysuhteen omaavat aurinkokennot valmistetaan III–V puolijohdemateriaaleista moniliitosrakenteella. Näiden aurinkokennojen toiminnan periaatteena on jakaa auringon spektri eri puolijohdekerroksille, mikä mahdollistaa aurinkokennon korkeamman hyötysuhteen sekä vähentää optisia ja termisiä häviöitä. Maailmanennätys hyötysuhde on saavutettu keskitettyä auringonvaloa hyödyntävällä III–V moniliitosaurinkokennolla. Kun auringonvaloa keskitetään edullisten optisten elementtien, kuten peilien ja linssien avulla, voidaan valmistaa hyvin pieniä aurinkokennokomponentteja, mikä laskee materiaalikustannuksia. Auringonvalon keskittäminen moninkertaistaa aurinkokennolle osuvan valon intensiteetin, mikä kasvattaa merkittävästi aurinkokennon tuottamaa sähkövirtaa.

Sähkövirran kasvu aiheuttaa aurinkokennossa tehohäviöitä, kun suurempi sähkövirta kulkee puolijohdekerroksista metallikontaktien kautta ulkoiseen kuormaan. Etukontaktia optimoimalla voidaan merkittävästi vähentää syntyviä tehohäviöitä. Etukontaktin kuviointi suunnitellaan siten, että virran kerääminen tapahtuu mahdollisimman tehokkaasti aurinkokennon etupinnalta. Samalla etukontaktin aiheuttama varjostusefekti tulee minimoida. Tyypillinen etukontakti muodostaa lineaarisen sormikuvion. Tässä diplomityössä perehdyttiin etukontaktin optimointiin kirjallisuusselvityksen sekä kokeellisen tutkimuksen avulla. Kokeellisessa osassa valmistettiin aurinkokennoja erilaisilla etukontaktin sormikuvioilla, joissa sormien välitys vaihteli 20 µm:sta ja 125 µm:iin. Tutkitut aurinkokennorakenteet kasvatettiin molekyylisuihkuepitaksialla ja aurinkokennokomponentit prosessoitiin fotolitografia-menetelmällä puhdastilaolosuhteissa. Valmistettujen aurinkokennojen karakterisoinnissa keskityttiin moniliitosaurinkokennon päällimmäisen alikennoon, sillä se toimii virranlevityskerroksena, jolloin etukontaktin vaikutus näkyy kaikista selkeimmin sen sähköisissä ominaisuuksissa. Aurinkokennojen virta-jännite-käyttäytyminen mitattiin yhden auringon sekä keskitetyn auringonvalon olosuhteissa, joista korkein saavutettu hyötysuhde oli 13,48%, kun konsentraatiokerroin oli 200 ja kontaktisormien välitys 75 µm. Samalla havaittiin, että aurinkokennojen sähköisiin ominaisuuksiin vaikutti merkittävästi konsentraatiokertoimen kasvattaminen erityisesti suuremmilla kontaktisormien välityksillä, minkä pääteltiin johtuvan merkittävästä tehohäviöistä verrattuna varjostusefektiin. Kun konsentraatio kasvatettiin 1000 aurinkoon, korkeimman hyötysuhteen tuotti kontaktisormien välitys 40 µm.

Etukontaktin optimointia tutkittiin myös MathWorks Simulink-ohjelmistoon perustuvalla simulaatiomallilla, jonka avulla pystyttiin laskemaan aurinkokennon sähköisiä ominaisuuksia keskitetyn auringonvalon olosuhteissa erilaisilla etukontaktien ominaisuuksilla. Simulaatiomallin tuottamien tulosten perusteella todettiin, että kontaktisormiin käytettävän metallin sähkön johtavuudella on sitä suurempi merkitys, mitä kapeampia ja matalampia kontaktisormia käytetään. Näin ollen hopea on varteenotettava metalli kontaktisormien valmistuksessa. Simuloitujen kontaktisormien mitat valittiin valmistusmenetelmien rajoitteiden mukaisesti.

Tämän diplomityön kokeellisessa tutkimuksessa onnistuttiin optimoimaan etukontaktin kuviointi kontaktisormien välitystä muuttamalla keskitetyn auringonvalon aurinkokennoihin. Saatujen tulosten perusteella voidaan valmistaa yhä tehokkaampia moniliitosaurinkokennoja ja tavoitella jopa yli 50% hyötysuhdetta.

Avainsanat: etukontaktikuvio, moniliitosaurinkokenno, III–V puolijohde, keskitetyn auringonvalon aurinkokenno, virta-jännite, karakterisointi

PREFACE

This thesis was conducted as a part of the solar cell research at Optoelectronics Research Centre (ORC) at Tampere University. I would like to express my gratitude to the examiner of this thesis, Prof. Mircea Guina, for giving me the opportunity to work among the most exciting fields of research. For the financial support, I would like to thank Fortum and Neste foundation.

Special thanks go to the examiner and the instructor of this thesis, Dr. Timo Aho. I value very much all the guidance and support I have received from you during these past few years. I would also like to thank Dr. Arto Aho, the instructor of this thesis, especially for the guidance through the results analysis. I want to acknowledge and thank Arttu and Leo from the solar cell team, for all the help, and for conducting the measurements and the simulations for this thesis. My office mates during the most of my time at ORC, Timo and Marianna, I would like to thank for making the work more fun I could have ever imagined. Finally, I want to acknowledge all my co-workers in the solar cell team and at ORC as well as the cleanroom team for, above all, providing the most enjoyable working environment.

In the end, I'm most grateful for the constant support from my parents and sisters. You are the reason I have made it this far.

Tampere, June 7th, 2021

Elina Anttola

CONTENTS

LIST OF SYMBOLS AND ABBREVIATIONS

AM	Air mass
ARC	Anti-reflection coating
ASTM	American Society for Testing and Materials
c-Si	Crystalline silicon
CB	Conduction band
CPV	Concentrated photovoltaics
HCPV	High concentration photovoltaics
IV	Current-voltage
LCPV	Low concentration photovoltaics
LPE	Liquid phase epitaxy
MBE	Molecular beam epitaxy
MOCVD	Metal organic chemical vapor deposition
ORC	Optoelectronics Research Centre
PV	Photovoltaics
VB	Valence band
VPE	Vapor phase epitaxy
η	Power conversion efficiency
λ	Wavelength of light
c	Speed of light
E	Photon energy
E_F	Fermi energy
E_G	Band gap energy
FF	Fill factor
h	Planck's constant
I_0	Dark saturation current
I_m	Maximum current
I_{ph}	Light-generated current
I_{SC}	Short-circuit current
J_{SC}	Short-circuit current density
k	Boltzmann's constant
n	Diode ideality factor
P_{in}	Incident power
P_m	Maximum power
q	Elementary charge
R	Resolution
R_P	Shunt resistance
R_S	Series resistance
T	Temperature
V	Applied voltage across the pn-junction
V_0	Equilibrium potential difference across the pn-junction
V_m	Maximum voltage
V_{OC}	Open-circuit voltage
W	Width of depletion region

1. INTRODUCTION

In the constantly warming climate, the development of renewable energy technologies is vital. One of the carbon-free energy solutions is solar photovoltaic (PV) technology. In fact, the production of PV devices has been rapidly increasing over the past couple of decades, and by the end of 2018, the total installed PV power capacity had reached approximately 520 GW [1]. In the same year, the PV technology also had the largest share of 39% of newly installed power capacity. Meanwhile, the power capacity covered by renewable energy sources had a portion of 25.6% of the total energy production. [1] It is clear that this number has to be increased to meet the goal of the 55% reduction of greenhouse gas emissions by 2030, set by the European Commission [2].

Individual PV elements, i.e., solar cells, are made of semiconductor materials. Semiconductors are a suitable choice for the fabrication of solar cells due to their electronic and optical properties. Conductivity of semiconductors can be increased by several orders of magnitude by applying external energy, for example, in the form of sunlight. The use of external energy excites electrons in the energy band structure of the semiconductor from the valence band (VB) to the conduction band (CB) which are separated by an energy gap defined by the band gap energy (E_g). [3] Therefore, E_g defines the wavelength of light that can be absorbed or emitted by the semiconductor.

Nowadays, most of the commercial PV devices are made of crystalline silicon (c-Si). Si has almost an ideal E_g with the value of 1.12 eV for the absorption of solar radiation when it comes to single-junction solar cells [4]. In addition, Si is both nontoxic and abundantly present in the form of oxides and silicates in Earth's crust which makes it an affordable choice for the PV technology. Lastly, manufacturing processes for Si-based materials are well-established and cost-effective since they are also widely used in other fields of semiconductor technology, such as microelectronics. [5] However, the absorption of solar radiation in the case of Si is limited by an indirect electronic transition from VB to CB, which limits the absorption coefficient that is generally higher for materials with a direct electronic transition. [6] Especially, many III–V semiconductors, such as GaAs, have a direct band gap, and can therefore be used to fabricate solar cells with higher power conversion efficiencies (η).

In the case of single-junction solar cells, there are fundamental limitations to maximum η based on the laws of thermodynamics. Theoretically, the upper-limit of η for a single-junction solar cell would be approximately 33.5% according to the Shockley-Queisser

efficiency limit. [7] To date, the record efficiencies for single-junction GaAs and Si solar cells in terrestrial use under the standard AM1.5G spectrum are 29.1 ± 0.6% and 26.7 ± 0.5%, respectively [8]. Single-junction solar cells suffer from transmission and thermalization losses. Incident solar radiation with energy exceeding E_g produces excess thermal energy. On the other hand, radiation with energy less than E_g cannot contribute to the energy conversion. [9] To reach higher values of η, III–V semiconductor materials are used to fabricate multijunction solar cells which utilize the solar spectrum over wider spectral range than single-junction solar cells. The operation principle of multijunction solar cells is to divide the incident solar spectrum between several active semiconductor layers with specified values of E_g which absorb optimally different parts of the solar spectrum [9]. Therefore, a higher η is obtained than what is possible for single-junction solar cells.

The efficiency of a solar cell can be further enhanced by using concentrated sunlight. In fact, concentrated photovoltaics (CPV) holds the current world-record efficiencies for different PV approaches: 27.6 ± 1.2% for Si solar cells and 47.1 ± 2.6% for III–V multijunction solar cells with six junctions [8]. Moreover, with a carefully optimized multijunction structure, an efficiency beyond 50% has been predicted [10]. In CPV, the intensity of the incoming solar radiation is typically increased by a factor between of 300× and 1000× in the case of high concentration PV (HCPV), whereas in low concentration PV (LCPV), the factor remains below 100× [11]. The general concept of the CPV system is presented in Figure 1.
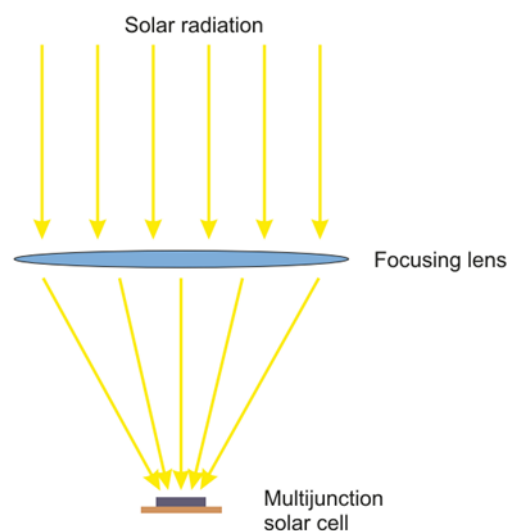

Figure 1. *The operation principle of the CPV system.*

When sunlight is concentrated using affordable optical elements such as Fresnel lenses and mirrors, the active area of the solar cell can be significantly reduced. This results in

considerable material and cost savings especially in the case of multijunction solar cells that are fabricated of rather expensive III–V semiconductors materials [12]. Furthermore, to utilize the concentrated sunlight as efficiently as possible, the CPV system typically includes a tracking system so that the vertical and the horizontal position of the optics and the solar cell unit relative to the direct component of the radiation is maintained [11].

There are many important aspects that need careful consideration when solar cells are illuminated with concentrated sunlight. For example, current generation in a solar cell scales linearly with the concentrator factor [12] which results in an increased series resistance. Resistive losses occur when current flows in the semiconductor layers of the solar cell, through the semiconductor-metal contact, and in the thin metallic contact fingers on the front side of the solar cell. A simplified structure of the solar cell is presented in Figure 2.
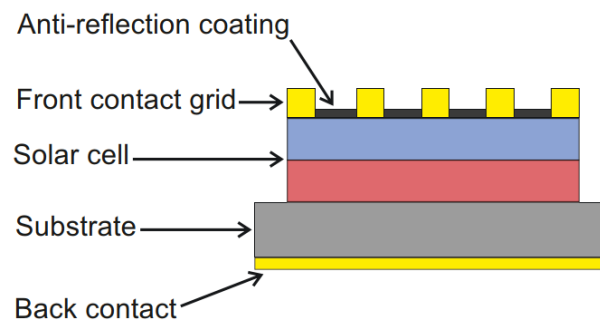
Figure 2.   *A simplified illustration of the typical solar cell structure.*

The series resistance is the most critical component decreasing η in HCPV applications [12, 13]. One way to reduce the series resistance is decreasing the contact finger spacing of the front contact grid. This thesis is focused on optimizing the front contact grid design for III– V semiconductor solar cells by varying the finger spacing and characterizing the electrical performance of the solar cells under concentrated illumination conditions. Another aspect of the optimization is the shadowing effect of the front contact that covers partially the solar cell surface preventing the incident sunlight from entering the semiconductor layers. In other words, the photon absorption is limited by the shadowing effect. Therefore, the balance must be found between the resistive losses and the shadowing effect to optimize the dimensions of the front contact. In this thesis, the front contact is optimized for CPV by designing, fabricating, and measuring CPV devices with different front contact designs. Measured results are analyzed against simulations, and a simulation tool is further used to investigate the optimal properties for the front contact.

The theoretical background of semiconductor solar cells is described in the next chapter including the properties of sunlight and the general electrical behaviour of semiconductor

solar cells. In addition, the basics of multijunction solar cells are introduced. Chapter 3 is focused on the considerations of the front contact grid. In the beginning, typical design geometries are introduced along with the main sources of power loss associated with the front contact. Then, the properties of metals use for the fabrication of the front contact are discussed. Lastly, a widely adapted photolithographic process for the fabrication of the front contact is described as well as alternative lithographic techniques that are used for the fabrication of more sophisticated front contact designs. The experiments conducted for this thesis along with the description of the utilized simulation tool are described in Chapter 4, and the results and analysis are provided in Chapter 5. Finally, the study that has been carried out for this thesis along with main results and prospective future aspects of further research on the topic are concluded in Chapter 6.

2. SEMICONDUCTOR SOLAR CELLS

In this chapter, the theoretical background of semiconductor solar cells is discussed. In the beginning, solar spectrum and properties of sunlight are considered, which support the understanding of the operation of solar cells. Secondly, the electrical behaviour of the solar cells and the key parameters to characterize the performance of the solar cells are introduced. In addition, resistive loss mechanisms are introduced as well as the operation of the solar cells under concentrated illumination conditions. In the final section, the concept of multijunction solar cells is considered.

2.1 Properties of solar radiation

The surface of the sun has a temperature of about 5762 K which can be closely approximated by a black body radiator [6]. The radiation intensity right above the Earth's atmosphere is known as solar constant and it has a value of 1366.1 W/m² [14]. However, in terrestrial applications, the effect of the Earth's atmosphere on the spectral distribution and intensity of the solar spectrum must be accounted for. A parameter called an air mass (AM) gives a path length of light passing through the atmosphere at certain location normalized to shortest possible path length which corresponds to the situation where the sun was directly on top [15]. The air mass is given by

$$AM = \frac{1}{\cos\theta},$$

(1)

where θ is the angle from the zenith (θ = 0°) [6]. Essentially, AM gives a measure of the atmosphere's effect on the spectral content and intensity of solar radiation. Significant absorption that impacts the solar radiation spectrum is caused by atmospheric gases including H_2O, O_3, CO_2, and CH_4. In addition, all molecules present in the atmosphere give rise to Rayleigh scattering at certain wavelengths that results in the blue color of the atmosphere as well as contributes to the extinction of solar radiation passing through the atmosphere. Other particles such as aerosols also affect the spectral content of solar radiation through absorption and scattering. [15]

For practical purposes, different AM numbers are defined to standardize the spectral content of solar radiation. With standardized spectra, the performance of solar cells from different manufacturers can be characterized and compared. The standard spectrum AM0 defines the spectral content just above the Earth's atmosphere and is designed for space applications. For terrestrial use, there are two standardized spectra for an air mass

of 1.5. One is an AM1.5G as a global spectrum normalized to the total power density of 1000.4 W/m^2 and the other is an AM1.5D as a direct spectrum normalized to 900.1 W/m^2 [16]. The AM1.5G includes both the direct and the diffuse component of the spectral content resulting from atmospheric effects whereas the AM1.5D includes only the direct component. The AM1.5G is designed for flat-plate applications under one-sun illumination whereas the AM1.5D is designed for concentrator applications. [15] The standard solar spectra AM0, AM1.5D and AM1.5G defined by the American Society for Testing and Materials (ASTM) [16, 17] with the visible spectrum as a reference are presented in Figure 3.
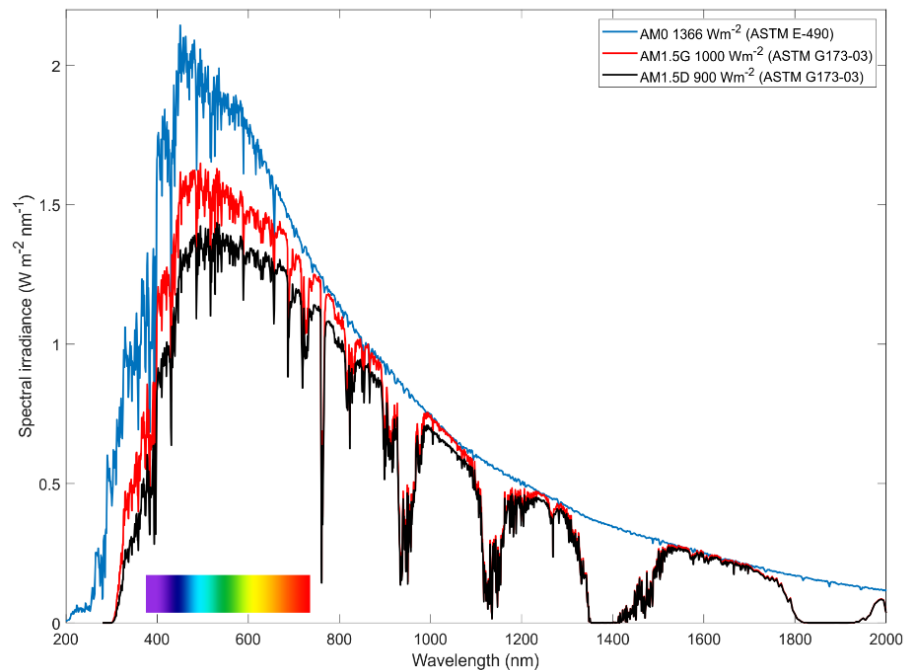
Figure 3. *Standardized ASTM solar spectra.*

Solar radiation is electromagnetic radiation that is generally characterized by its frequency v or, alternatively, its wavelength λ [6]. Electromagnetic radiation is quantized which is described by photon particles. Each photon carries an amount of energy E given by

$$E = hv = \frac{hc}{\lambda},\qquad(2)$$

where h is Planck's constant and c is the speed of light. [18] The photon energies can be used in the case of semiconductor solar cells, only if $E \geq E_g$ in which case it can create an electron-hole pair, and, thus, contribute to the energy conversion process [6]. Solar radiation spectrum is one of the key aspects especially when multijunction devices are designed so that the whole spectral range can be utilized as efficiently as possible.

2.2 Electrical properties of solar cell

Doped semiconductors are essential materials for fabricating solar cells. By doping, excess carriers are introduced to the semiconductor crystal structure. Semiconductor material can be either p- or n-doped. For example, when P from group V is introduced to Si, there is an extra electron in the structure for every added P atom. In this case, the P atom is called a donor and it makes material n-type. On the other hand, B from group III in Si structure would act as an acceptor adding an extra hole which makes material p-type. [3] For GaAs, Si is a typical n-type dopant and Be a p-type dopant [19].

A pn-junction is the key structure in the operation of a solar cell [6]. Figuratively, the a pn-junction is formed when p- and n-type semiconductor materials are brought together. Because of the doping, there is a difference between electron and hole concentrations across the pn-junction. Therefore, the majority carriers from the n-type material, electrons, diffuse into the p-type region and vice versa. This results in ionized donors and acceptors on their respective sides at the junction. The oppositely charged ions produce an electric field with a direction from n-side to p-side. The electric field opposes the flow of charge carriers due to diffusion. On the other hand, the minority carriers, electrons from the p-side and the holes from the n-side, are swept across the junction due to the electric field. Diffusion and drift of carriers create the components of electrical current flow in the semiconductor structure. The presence of the electric field creates a depletion region across the pn-junction since there are very few mobile charge carriers within this region at any given time. The width of the depletion region is given by W. Outside the depletion region, material remains mainly charge neutral. These regions are generally called a base and an emitter. At thermal equilibrium, the net current flow is zero and there is an equilibrium potential difference V_0 across the junction. Because of V_0, the energy bands bend so that they are higher on the p-side by the amount of qV_0. Potential difference acts as a barrier for the diffusion of majority carriers. [3, 6] A generalization of the structure of the pn-junction and the energy band alignment are shown in Figure 4. The E_F represents the Fermi level energy. The concept of the Fermi level arises from the fundamentals of Fermi-Dirac statistics [3].
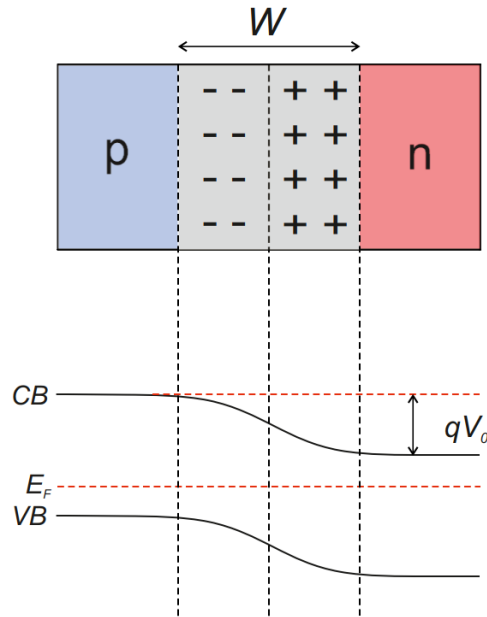
Figure 4. *A generalized structure of a pn-junction and the corresponding energy band alignment.*

When an external voltage is applied across a pn-junction, the balance between diffusion and drift components of the current shifts. Correspondingly, the applied voltage affects the energy band alignment. Under forward bias, the potential barrier is lowered, and more majority carriers can diffuse across the junction, which increases the diffusion current. Under reverse bias, on the other hand, the potential barrier is increased, and the diffusion becomes negligible. However, the reverse bias enhances the electrical field across the junction, thus, the drift of minority carriers gives rise to the drift current that is independent of the applied voltage because of the small amount of minority carriers on the both sides of the junction. Thus, in the ideal case, the current-voltage (IV) characteristics of an unilluminated pn-junction (dark IV) can be represented by the diode equation:

$$I = I_0 \left(e^{\frac{qV}{nkT}} - 1 \right), \tag{3}$$

where I_0 is called dark saturation current, V is the voltage across the junction, q is the elementary charge, n is the diode's ideality factor, k is the Boltzmann's constant, and T is the temperature. [3] The dark IV curve is shown in Figure 5 with a dashed line.

When a solar cell is illuminated with solar radiation, the diode characteristics described above change. The absorption of photons in a solar cell creates light-generated carriers. Both majority and minority carriers are created while, however, the number of minority carriers is increased significantly relative to majority carriers already present in the doped regions. Therefore, the light-generated current (I_{ph}) can be approximated by the number

of minority carriers created due to illumination. [6] The diode equation describing the current flow in a solar cell becomes

$$I = I_0 \left(e^{\frac{qV}{nkT}} - 1 \right) - I_{ph}. \tag{4}$$

The form of Equation 4 shows that the illumination creates an additional reverse current component which shifts the IV curve by the amount of I_{ph} into the fourth quadrant of the coordinate system. This means that power can be extracted from the solar cell. [3] The IV curve of the solar cell under illumination with respect to the dark IV curve of a diode are shown in Figure 5.
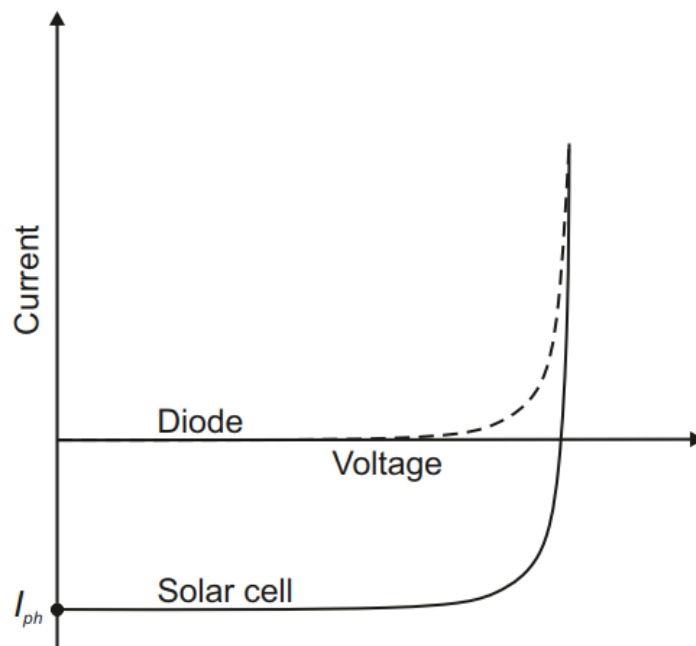
Figure 5. *IV characteristics of solar cell with respect to diode characteristics in dark. Typically, $I_{ph} \gg I_0$. Adapted from [20].*

2.2.1 Current-voltage characteristics

There are a few important parameters that can be extracted from the IV curve which are commonly used to characterize the electrical performance of the solar cell. These parameters include the short-circuit current (I_{SC}), the open-circuit voltage (V_{OC}), the maximum power (P_m), the fill factor (*FF*), and η. These parameters are illustrated in the characteristic IV curve for the solar cell in Figure 6. In addition, the short-circuit current density (J_{SC}), that is derived by dividing I_{SC} by the area of the solar cell, is often defined to cancel the current dependency on the area of the solar cell.
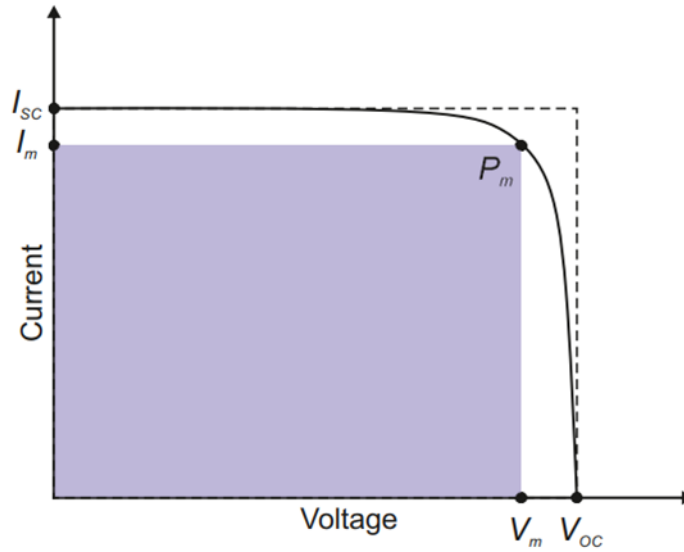
Figure 6. *The characteristic IV curve for the solar cell. Adapted from [20]*

For convenience, current is usually presented in the positive y-axis. The point where the curve crosses the y-axis is defined by I_{SC}. Ideally, I_{SC} is equal to I_{ph}. At this point the voltage across the solar cell is zero and all current flows to the external load. When the voltage increases to a certain point, the current changes rapidly and the point where the curve crosses the x-axis is defined by V_{OC}. At this point, all light-generated carriers re-combine and no current flows to the external load. The open-circuit voltage is given by

$$V_{OC} = \frac{nkT}{q} \ln\left(1 + \frac{I_{SC}}{I_0}\right). \tag{5}$$

Since typically $I_{SC} \gg I_0$, V_{OC} can be approximated as

$$V_{OC} \approx \frac{nkT}{q} \ln\left(\frac{I_{SC}}{I_0}\right). \tag{6}$$

Furthermore, P_m is the maximum power that can be extracted from the solar cell, and it is given by the maximum power point on the IV curve which is defined by the values of the maximum current (I_m) and the maximum voltage (V_m). This can also be illustrated by *FF* that defines the largest rectangle under the IV curve whose area is given by $P_m = I_m V_m$. In addition, *FF* gives the ratio of the two rectangles illustrated in Figure 6: the one defined by the maximum power point and the other defined by I_{SC} and V_{OC}:

$$FF = \frac{I_m V_m}{I_{SC} V_{OC}} = \frac{P_m}{I_{SC} V_{OC}}. \tag{7}$$

The ratio of Equation 7 has a value always less than 1 in the case of real solar cells. From the practical point of view, *FF* is a measure of the quality of the solar cell. The value of *FF* is affected by parasitic resistive losses due to material and structural properties of the solar cell.

Finally, probably the most used parameter to characterize the performance of solar cells is the power conversion efficiency which is given by

$$\eta = \frac{P_m}{P_{in}} = \frac{I_{SC}V_{OC}FF}{P_{in}}. \tag{8}$$

Essentially, η defines the ratio of the maximum output power from the solar cell to the incident power (P_{in}) in the form of the solar radiation. [6, 20]

2.2.2 Resistive losses

When the operation of real solar cells is considered, parasitic resistive effects must be accounted for. Resistance can appear in series or in parallel to the current flow in the solar cell. The series resistance (R_S) arises from lateral and vertical current flow in the structure including semiconductor layers and contact electrodes. Parallel resistance, also called the shunt resistance (R_P) typically arises from crystalline defects acting as current shunts which can be created during the fabrication process of the solar cell. [9] The effect of R_S and R_P on the IV characteristics of the solar cell is shown in Figure 7.
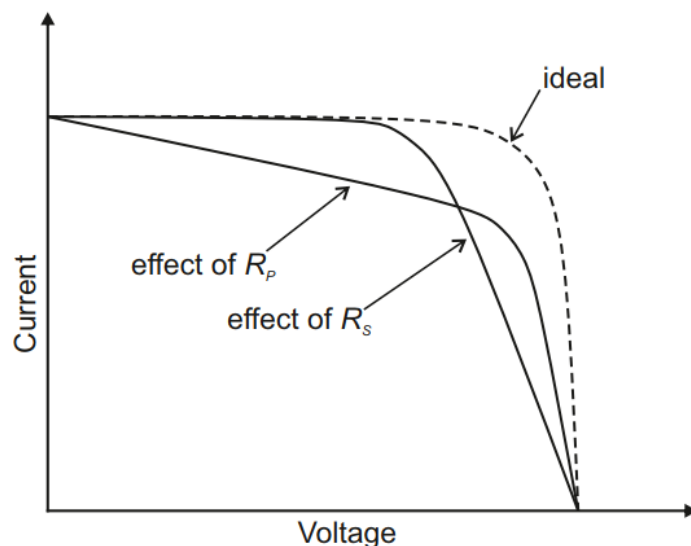
Figure 7. *The effect of resistive components on the ideal IV characteristics of the solar cell. Adapted from* [20].

Essentially, parasitic resistances result in the decrease of *FF*, which can be observed from the shape of the IV curves with R_S and R_P in Figure 7 compared to the ideal case.

For an ideal, lossless solar cell, the values of resistive components would be $R_S = 0$ and $R_P = \infty$ [21]. Resistive losses become more evident in complex heterostructures, such as multijunction solar cells. Therefore, the fabrication process of these structures is challenging since resistive losses may significantly degrade the performance of the solar cells. Moreover, enhanced current generation in the solar cell under concentrated illumination conditions gives rise to the increase of R_S. The aspects of the solar cell operation under concentrated conditions is discussed in more detail in the following section.

2.2.3 Operation under concentrated conditions

The general electrical behaviour of the solar cell is affected by illumination with concentrated sunlight. As shown in Equation 5, V_{OC} is logarithmically dependent on the current. Therefore, as the current increases linearly with the concentration factor [9], the theoretical corresponding increase in V_{OC} is of several kT/q. As a result, increase of η is also logarithmic with the concentration factor as can be observed from Equation 8 where the linear increase of both I_{SC} and P_{in} with the concentration factor cancel each other. The increase in η is even more evident in series-connected multijunction devices since voltage of each sub-cell is additive [21]. As a result, each sub-cell will contribute to the net increase of V_{OC}.

In practice, the effect of higher operation temperatures and increased current generation in the solar cell due to concentration need careful consideration. In general, the band gap is temperature-dependent according to Varshni's empirical expression [20], which leads to the reduction of the band gap as temperature rises. The reduction results in a shift in absorption bands to longer wavelengths in sub-cells which needs to be accounted for when solar cells for concentrator use are designed and fabricated. In addition, V_{OC} also decreases when temperature is increased [22], which was experimentally observed in [23]. This phenomenon limits the efficiency of the solar cell under concentration unlike what could be predicted by theoretical observations. In practice, heating effects can be reduced by using different cooling systems. For example, passive cooling is used for single solar cells by mounting them on heat distributors made of a material with good thermal conductivity such as aluminum or copper. On a module-level, active heat distribution is required which is achieved by an integrated external cooling cycle with air or fluid circulation. In such system, thermal energy can be utilized. [22]

Lastly, loss mechanisms due to increased current production under concentration must be considered when designing solar cell devices. Power losses arise from series re-

sistance in semiconductor layers, contact fingers, and at the semiconductor-metal inter-
face. The optimization of the front contact grid design is required to reduce power losses
in CPV which will be further discussed in the later chapters.

2.3 III–V multijunction solar cells

To enhance the efficiency of a single-junction solar cell, a solar cell with multiple junctions
is introduced. The operation principle of the multijunction solar cell is illustrated in
Figure 8.

$$E \geq E_{g1} \quad E \geq E_{g2} \quad E \geq E_{g3} \quad E \geq E_{g4}$$

$$E_{g1}$$
$$E_{g2}$$
$$E_{g3}$$
$$E_{g4}$$
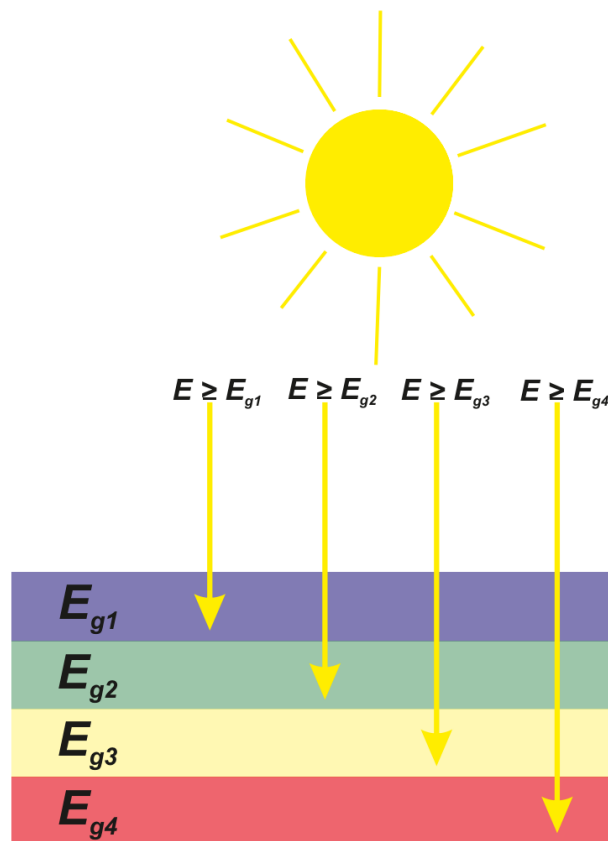
Figure 8.   *The operation principle of the multijunction solar cell.*

The key concept of multijunction solar cells is to operate with a wider spectral range than
what is possible for single-junction solar cells, which results in higher η. In principle, light
is absorbed for photons with energy $E \geq E_g$. However, the energy exceeding the E_g
causes thermalization losses, which is the major issue for single-junction solar cells. In
multijunction approach different spectral regions are absorbed in separate semiconduc-
tor layers with specified values of E_g. There are a wide variety of III–V compound semi-
conductor materials suitable for the fabrication of multijunction devices. Many III–V
compounds have direct band gaps ensuring efficient absorption of light. In addition, by

varying elemental composition of an alloy, E_g can be tuned to absorb a certain range of the solar spectrum. [24]

A stacked arrangement is a conventional way to compose the multijunction solar cell. In this approach, sub-cells are stacked with a decreasing order of values of E_g from top to bottom. In other words, sub-cells act as optical filters by distributing the spectrum within the structure. The stacked structure can be constructed in different ways, for example, by simple mechanical stacking, by wafer bonding, or by monolithic growth on a single substrate [20].

The monolithic structure of the multijunction solar cell can be grown either lattice-matched or with a metamorphic architecture. In the lattice-matched structure the lattice constants of the sub-cells and the substrate have the same value, whereas the metamorphic approach requires buffer layers to be grown between the sub-cells to gradually alter lattice-constants. [21] Otherwise, the mismatch of lattice constants would result in a strained structure and, eventually, cause dislocations and degrade the overall quality of the crystal. Lattice-matching results in material savings since it does not require buffer layers. Another advantage of the lattice-matched structure is that only one type of a tunnel junction between the sub-cells is needed, while in metamorphic structure several tunnel junction designs are required because of the variation in lattice-constants. In general, tunnel junctions connect the sub-cells electrically while having minimal resistance to the current flow, and they maintain the right polarity to the diode-like operation of the solar cell. In addition, tunnel junctions are made of large band gap materials which make them optically transparent, thus, they don't produce absorption losses. [24, 25] Evidently, the lattice-matched structure is more straightforward to construct. However, since the metamorphic approach doesn't require lattice-matching, there are a wider variety of materials available for the fabrication of metamorphic multijunction solar cells. As a result of the monolithic construction of the multijunction solar cell, the sub-cells are connected in series. Therefore, the current production of the device is limited by the sub-cell generating the least current. Consequently, all sub-cells should produce approximately the same amount of current which is also called a current-matched condition. [9]

Epitaxial crystal growth methods are used to fabricate multijunction solar cells with very high crystalline and optoelectronic quality. In principle, epitaxy is a highly controllable growth method where monolayers are deposited with the crystalline orientation of the substrate. Moreover, precise doping profiles can be achieved by epitaxy. Epitaxial growth techniques include liquid phase epitaxy (LPE), vapor phase epitaxy (VPE), metal organic chemical vapor deposition (MOCVD), and molecular beam epitaxy (MBE), of which

MOCVD and MBE are most common methods to fabricate monolithic, complex hetero-structures such as multijunction solar cells [24, 26]. Epitaxial growth in MBE occurs in a chamber that is capable achieving ultra-high vacuum ($\sim 10^{-10}$ mbar) conditions which is ensured, for instance, by different vacuum pumps and liquid nitrogen cooling. The elements for the crystal structure and possible dopants are kept in crucibles. When the crucibles are heated and shutters placed in front of them are opened, atoms travel directly onto the heated substrate of which lattice structure the growing semiconductor layer is adopting. Mechanical shutters and precise temperature control enable highly controlled deposition of monolayers of different composition. In addition, the heated substrate is typically rotated to make the growth as uniform as possible. [27] MOCVD, on the other hand, is based on chemical reactions between gaseous molecules that contain elements for the crystal growth. For example, the chemical reaction between $Ga(CH_3)_3$ and AsH_3 gases is used to grow GaAs. The MOCVD growth can occur in atmospheric pressure or in low pressure. [26]

In practice, the fabrication of the complex multijunction solar cell structures involves several important aspects. The band gaps of the sub-cells should match the solar spectrum while the high crystal quality and the performance of the device are maintained. Moreover, material parameters such as doping levels and charge carrier lifetimes as well as processing-related aspects including the design of the front contact grid and anti-reflection coating (ARC) affect the performance of the device. An example of a state-of-the-art device is a lattice-matched four-junction solar cell with the structure consisting of AlGaAs, GaAs, and two GaInNAsSb sub-cells having values of E_g of 1.9 eV, 1.4 eV, 1.2 eV, and 0.9 eV, respectively. [10] With bottom cells including dilute nitride materials, even the lowest energies, or correspondingly the longest wavelength range of solar spectrum can be covered.

III–V multijunction solar cells have applications both in space and in terrestrial concentrator systems. In space, an excellent radiation resistance and low temperature coefficients of III–V semiconductors is needed for satellites and space stations [28, 29], and at the moment, III–V semiconductor solar cells are the dominant power source for space applications. In CPV systems, the high optoelectronic quality of III–V multijunction solar cells is essential. Multijunction solar cells are suitable for CPV technology for several reasons. Firstly, the overall efficiency provided by multijunction solar cells is much higher than for other PV technologies [30], which is proven by the world record efficiency. In addition, because the required area of solar cell is significantly reduced in CPV, multijunction solar cells are a cost-effective choice. Moreover, the operation of a multijunction solar cell typically occurs at high voltage rather than high current which diminishes

the effect of ohmic power losses. Lastly, lower temperature coefficients of multijunction solar cells compared to other PV technologies make them suitable for higher operation temperatures of CPV. [12]

3. FRONT CONTACT GRID

The design of the front contact grid for solar cells, which is the objective of this thesis, involves several aspects, such as the dimensions of the front contact affecting the balance between resistive and shadowing losses, material choices, and limitations set by fabrication techniques. Furthermore, in concentrator use, raised current densities must be accounted for.

In this chapter, the main prospects of the front contact design for CPV are considered. In the beginning, the main sources of power loss due to the front contact grid are introduced. Then, different approaches for the front contact design for CPV are presented. Then, the typical photolithographic fabrication process of the front contact for high-efficiency CPV solar cells is described. Finally, alternative lithographic techniques are briefly discussed.

3.1 Design considerations

There are several approaches for the front contact grid design. For HCPV, the typical grid geometry is a linear grid design [9, 12, 31-33]. Another common design is a so-called inverted square geometry [13, 32, 34]. These design geometries are illustrated in Figure 9.
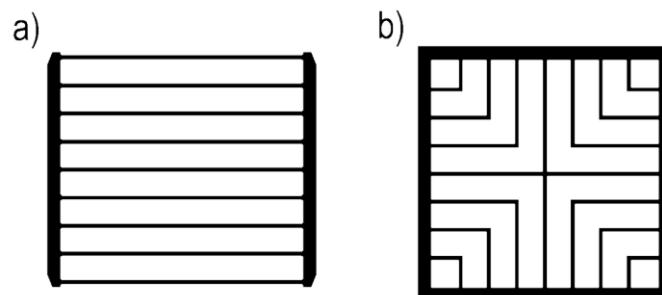
Figure 9.   *a) Linear and b) Inverted square grid design.*

As shown in Figure 9, the thin contact fingers allow for even and efficient charge carrier collection over the whole surface area of the solar cell. Then, current is extracted from the busbars on the sides. For the linear design, the typical periodicity for contact fingers in mm^2-scale CPV solar cell components is in the order of 100 µm, whereas the typical width of contact fingers is in the order of a few micrometers [13, 31, 33, 35]. Front contact grids with such dimensions are commonly manufactured by photolithography methods. When the two designs are compared, it is observed that the distance for the carriers to

travel from the collection point to the busbar varies significantly. For example, the longest distance for the carrier to travel to the busbar is equal everywhere on the vertical line in the center of the linear design. In the case of the inverted square design, the longest travelling distance to the busbar is only for carriers that are collected at the center point of the active area. In addition, current is collected at all four sides of the solar cell due to the busbar design. Therefore, it could be argued that the carrier collection and extraction of the inverted square grid may be more efficient. However, the linear grid design, which was studied in this thesis work, is probably more straightforward to fabricate as well as to model.
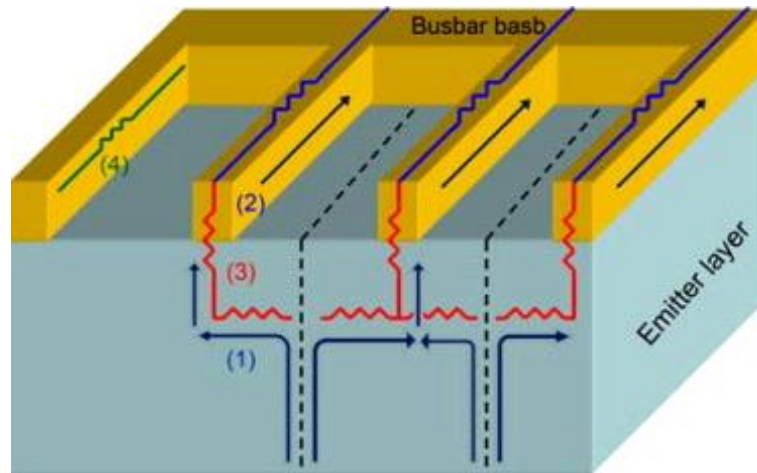
3.1.1 Loss mechanisms

The design of the front contact grid is based on finding the balance between series resistance and the shadowing effect in CPV applications. In principle, decreasing the contact finger spacing lowers resistive losses both in the top emitter layer and in the metallic contact fingers. However, as the metal area covering the front-surface of the solar cell increases, less photons are transmitted into the active layers of the solar cell. According to [31], the shadowing effect dominates the total power losses in LCPV applications. However, at higher concentration levels, the resistivity of the contact fingers becomes the dominating source of total power losses and, thus, the optimization between power losses and shadowing effect is required. There are four main power loss mechanisms related to the front contact grid due to

1) Sheet resistance of the top emitter layer
2) Metal contact finger resistivity
3) Contact resistance at the metal-semiconductor junction
4) Shadowing. [31]

These loss mechanisms are illustrated in Figure 10.

Figure 10. Power loss mechanisms due to the current flow in a solar cell [31].

3.1.2 Metals

In addition to the geometry, the design of the front contact also involves careful consideration of used metals. Properties, such as electrical resistivities of different metals, chemical compatibility in the fabrication process, cost-effectiveness, and their ability to form ohmic contacts to semiconductor must be accounted for.

In order to extract the generated current effectively from the solar cell, metallic contact-electrodes are fabricated on the back and on the front of the solar cell. Electrons enter an external circuit through the one electrode and arrive back filling the holes on the VB through the other. On the back, the contact can cover the whole surface. However, on the front the contact geometry must be designed in a way that the semiconductor surface is only partially covered so that light can be absorbed.

The junction that is formed between metal and semiconductor can have rectifying characteristics due to a potential barrier formation which is called a Schottky contact. Alternatively, the contact can be ohmic with linear IV characteristics across the junction which results in minimal resistance. The latter is preferred in the case of solar cells. In theory, the junction formation to III–V semiconductors results rarely in ohmic contact due to the position of surface states of semiconductor within the band gap and Fermi-level alignment. Thus, a potential barrier limits the flow of majority carriers across the junction. However, the width of the potential barrier can be reduced by doping the semiconductor heavily under the contact area. In this case the charge carriers can tunnel through the potential barrier with an increased probability. [3, 36]

The properties of the metal-semiconductor junction are also affected by the purity of the semiconductor surface prior to metal deposition, the choice of metals, and the deposition

technique. Native oxides are formed onto the surface of the semiconductor when it is exposed to ambient air. The oxide layer impedes the formation of an ohmic contact. Thus, an additional oxide removal step is usually employed prior to metal deposition. [37] Metal stacks such as Ti/Pt/Au and Ni/Au are usually utilized in the contact electrodes of solar cells instead of single metal because of their better properties of forming ohmic contacts and good adhesion to semiconductors [33, 37]. In addition, certain metal stacks are utilized to prevent the diffusion of metals into the semiconductor or vice versa.

For high efficiency devices, such as III–V multijunction solar cells for CPV, contact electrodes are typically fabricated from noble metals, such as Au and Ag because of their superior conductivities over other metals and the simple integration into fabrication processes. However, the use of noble metals should be considered carefully for commercial mass production due to the high price. A potential alternative metal could be Al that is more affordable and has sufficiently low resistivity [34]. However, an assessment of different front contact grids made of different metals has been conducted, and it was concluded that Au- and Ag-based front contacts had better performance over Al at high concentrations up to 800× [38].

3.1.3 Advanced designs

The light management aspect of the solar cell design has become more essential to further improve the broadband absorption of sunlight and to compensate optical losses. Especially the emerging field of thin film solar cells can benefit from advanced light trapping schemes. In general, light trapping is utilized to enhance the path length of light in the absorbing layers, for example, by scattering, by diffraction, or by internal reflections. In thin film solar cells, the active light absorbing layer is reduced to orders of micro- or even nanometers [39]. For comparison, a traditional c-Si solar cell requires the thickness of an active absorbing layer of > 100 µm for sufficient absorption of sunlight [40]. The thick absorbing layer increases the probability of charge carriers to recombine before reaching the contact electrodes. The reduction of the thickness of the active layer leads to significant material savings. In addition, the current collection efficiency can be further improved because of reduced travelling distances for charge carriers. At the same time, absorption losses become more significant which can be compensated by light trapping. Because of fundamental limitations of Si, higher values of η can be reached by integrating light trapping structures into thin film GaAs solar cells [39] as well as multijunction solar cells [41].

There are several approaches to realize a light trapping structure in solar cells. It can be integrated in a solar cell's back contact as planar or structured back reflectors reflecting

the passing light back into the active layers which increases the probability of light to be absorbed [42]. Alternatively, deposited metallic nanoparticles can act as light scatterers on the surface of a solar cell [40, 43]. Light scattering and diffraction can also be utilized by dielectric or semiconductor surface texturing [44, 45]. Lastly, a light trapping structure can also be integrated into the front contact of the solar cell as a metal nanogrid [46, 47]. In the case of the front contact, an advanced nanoscale design can significantly compensate the shadowing losses while maintaining high electrical conductivity compared to more traditional approaches. Metallic nanostructures produce plasmonic effects that is produced by electronic oscillations in a metal [48]. When incident light has a specific resonant frequency, a strong collective oscillation of electrons occurs in a metal which results in either absorption or scattering of light. Scattering becomes dominant effect in case of metal structures with dimensions approximately of 100 nm or larger. Scattered light couples strongly into the semiconductor enhancing the absorption. [48] It has been reported that a Ag nanogrid based on plasmonic effects and with carefully designed dimensions can have light transmission up to 91% while maintaining high electrical conductivity [47]. Such approach is an attractive choice also for solar cells.

However, there is barely any research of such front contact designs in CPV. The reason for this might be that reaching higher values of η do not yet require sophisticated light management while research is still focused on the development of growth techniques and materials. Another issue with a nanoscale front contact design for CPV might be that the conductivities do not match the high current densities which would need more research efforts. Yet, an alternative front contact design approach with trapezoidal grid fingers has also been demonstrated on CPV to decrease the shadowing losses and enhancing FF and V_{OC} at high concentration levels [35]. Furthermore, microscale contact fingers with triangular cross-section could act as "effectively transparent" front contacts by redirecting incoming light efficiently into active semiconductor layers. This approach has been reported to significantly reduce the shadowing losses, reflection and parasitic absorption in metals while maintaining high conductivity. [49]

3.2 Principles of lithography

Photolithography followed by metal deposition and lift-off is a typical process-flow for the fabrication of the front contact grid for high-efficiency concentrator solar cells. With this fabrication process, contact fingers with widths of the order of micrometers can be achieved. [9] High quality contact electrodes are commonly deposited by vacuum evaporation techniques such as electron-beam (e-beam) or thermal evaporation [37, 50]. With

the lift-off process, extra metal layer with the underlying photoresist is removed with an appropriate photoresist stripper or solvent.

3.2.1 Photolithography

The principle of photolithography is to transfer an image pattern on a photomask on to a sample coated with a photoresist, a photosensitive polymer [51]. When the sample is exposed through the photomask, typically with light near the UV-range in the case of photolithography [51], the unmasked part of the photoresist is exposed. The exposure alters the chemical properties of the photoresist. In the case of a positive photoresist, the exposed areas become soluble in a certain type of developer solution. The exposed areas of a negative photoresist, on the other hand, become cross-linked while the unexposed parts remain soluble in the developer. [52] With carefully considered steps of photolithography, a suitable photoresist patterning can be prepared for the following processing steps including metal evaporation and the lift-off process. Important aspects of photolithography include the thickness of the deposited photoresist layer, the resolution of the produced pattern, and the profile of sidewalls of the openings in the photoresist pattern. In general, an undercut photoresist sidewall profile is required for the lift-off process which can be achieved with negative or image-reversal photoresists [52]. A typical photolithographic process flow for the fabrication of the front contact grid is presented in Figure 11. This process flow has also been used in the experimental part of this thesis in the solar cell processing.
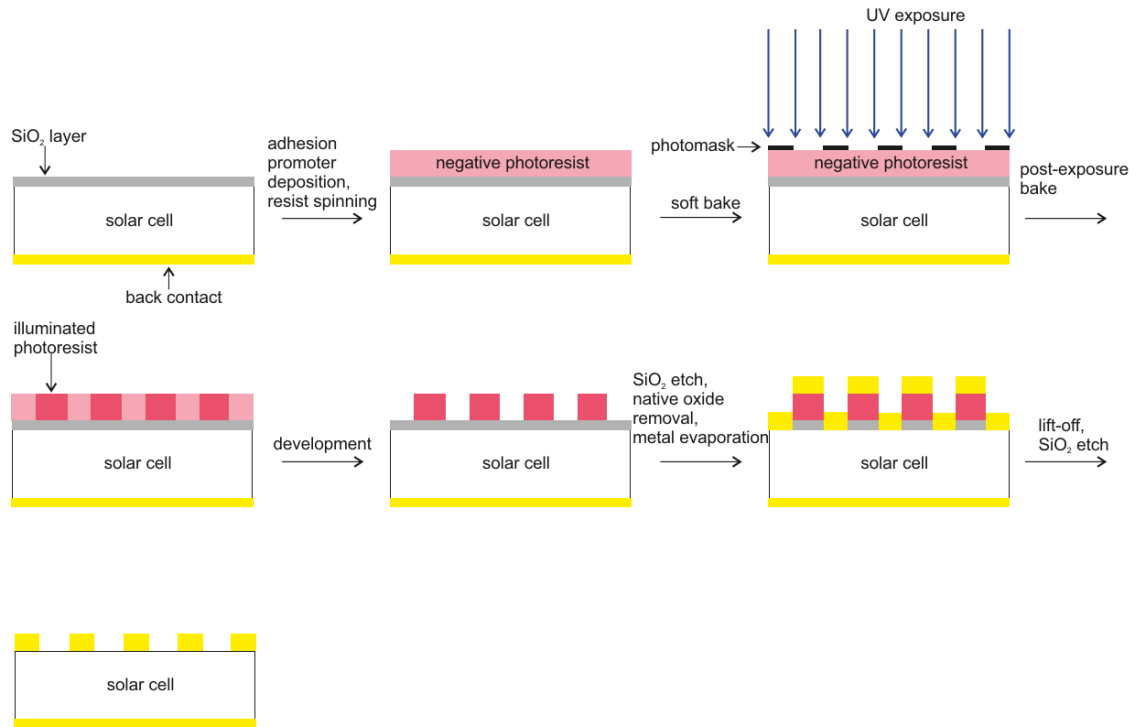
Figure 11.   *A typical photolithographic process flow for the fabrication of the front contact grid.*

If features closer to nanoscale are wanted to be produced, for example in the case of more advanced front contact designs, photolithography has some fundamental limitations regarding the resolution. Ultimately, the wavelength used for exposure sets a limit to pattern resolution due to diffraction. In principle, resolution (R) can be derived from the Rayleigh criterion [53]:

$$R = k_1 \frac{\lambda}{N_a}.$$

(9)

In Equation 9, k_1 is a process-dependent constant, λ is the wavelength of light used for the exposure, and N_a is the numerical aperture of the imaging system. However, the expression of Equation 9 does not give the exact value of resolution in photolithography since it assumes a point-source of light which is not the case in reality. In addition, also other factors of photolithography process affect the resolution, such as, the photomask and the chemical properties of the photoresist. However, the Rayleigh expression gives the right order of magnitude for the value of R limited by diffraction. Therefore, R can be further improved by using shorter wavelengths.

Some typical light sources for photolithography are mercury vapor lamps operating at 436 nm, 405 nm, or 365 nm wavelengths. To further reduce the feature size, UV-emitting lasers have been used which operate at 193 nm, for example. A notable benefit with

lasers is that they operate at very narrow spectral range. [51] Finally, extreme-UV lithography operating at 13.5 nm has also been reported [54]. However, the challenge impeding the development of this technology is that many materials, including air, are strongly absorbing at this wavelength. Therefore, the whole optical system should be enclosed in a near-vacuum-environment which would significantly increase the cost of the system. [53] An alternative approach to obtain nanoscale feature sizes is to use other lithographic techniques such as nanoimprint (NIL) or e-beam lithography which don't suffer from optical limitations.

3.2.2 Other lithographic techniques

With e-beam lithography, features with dimensions of 10 nm or smaller can be produced with a high precision. E-beam lithography is based on a direct-write method which does not require a mask during the exposure of the resist which makes the procedure more straightforward. Typically, electrons with energies of 5-100 keV are used corresponding extremely short wavelengths, thus, diffraction would occur only from features with atomic dimensions. On the other hand, since electrons are scattered by solids, the resolution is limited by the beam broadening due to scattering in the resist. The use of higher energy of electrons ($>$ 50 keV) decreases scattering, but energy gets deposited onto the substrate which may lead to thermal expansion and quality degradation. A final important consideration is that the procedure is conducted in a vacuum-environment and the writing times are significantly longer than in optical techniques. Therefore, e-beam lithography is more suitable for research and prototyping rather than high-volume production of solar cells at present. [53] E-beam lithography has already been demonstrated in the solar cell research to develop sophisticated front contact designs [46, 47, 55, 56].

NIL is another technique to form features of nanoscale ($<$ 1 μm) on a substrate. NIL is a non-projection technique that does not require the use of photomasks and it does not involve the exposure of the resist polymer with photons or electrons. Therefore, the technique does not suffer from defects due to optical diffraction or scattering. Instead, a pattern is first prepared on a physical template made, for example, of glass, nickel, or silicon, from where it is transferred onto a substrate. The first step of the patterning occurs when the template is brought into contact with a substrate covered with a suitable polymer. For a metallization process, the conventional way is to use a transparent template that allows for the polymer to be hardened using UV light. Once the pattern is transferred, openings into the polymer are etched to uncover the surface of the substrate. Then, metals are evaporated and finally, the lift-off process is applied to remove residual metals and polymer. From the production point-of-view, NIL is an attractive technique since it does not

require expensive optical systems or a vacuum-environment which makes it much more affordable. In addition, it provides a higher production throughput of nanostructures than e-beam lithography, for example. However, the mechanical nature of NIL makes it prone to defects because even smallest errors on a template get transferred onto the substrate which may be problematic especially in high-precision semiconductor device applications. [53, 57]

4. EXPERIMENTAL METHODS

The experiments for this thesis were conducted at ORC at Hervanta-campus of Tampere University. III–V semiconductor solar cells were grown by the GEN20 MBE system (Veeco). Solar cell processing was conducted in cleanroom facilities. In this work, the linear front contact grid design was investigated in more detail. The solar cell devices were fabricated with eight different contact finger spacings ranging from 20 μm to 125 μm. Then, the electrical performance of the solar cells was characterized with one-sun and concentrated IV measurements. Solar cell processing and the setup for the IV measurements are described in detail in Chapters 4.1 and 4.2, respectively.

In Chapter 4.3, simulations for modelling the electrical performance of the fabricated solar cells are introduced. Simulated results were compared to the results obtained from the IV measurements. Furthermore, the simulation model was utilized to optimize the dimensions and the structure of the front contact grid under chosen concentration level.

4.1 Solar cell processing

Solar cell devices were prepared by using photolithography. Photolithographic steps were utilized for the fabrication of the front contact grid as well as for defining and etching the mesa structure, and the deposition of ARC. Prior to the processing of the solar cells, a new photolithography mask was designed and drawn with AutoCAD 2018 software. In Figure 12, partial masks for different photolithography steps are shown with different colors: red indicates the mesa boundaries, yellow the front contact grid, and blue the ARC.
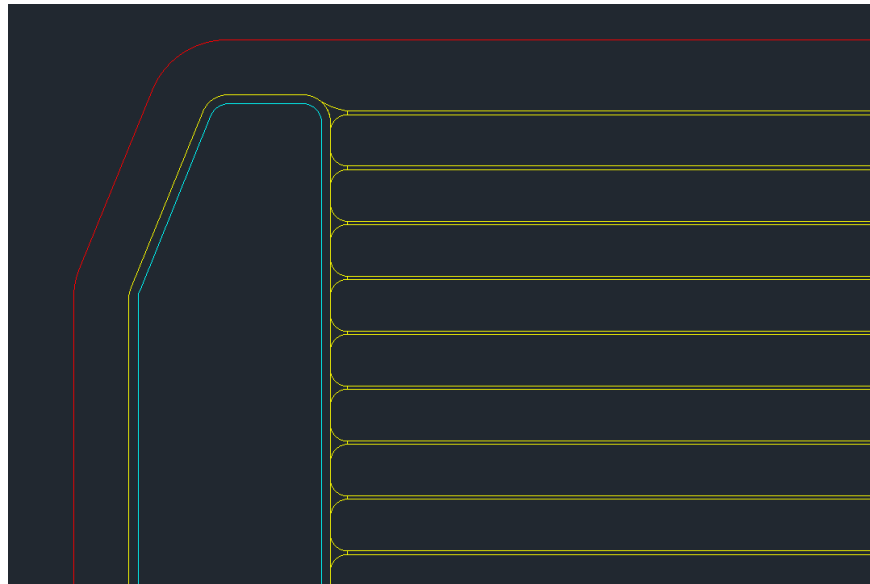
Figure 12. *The photolithography mask design.*

For practical reasons, as it is shown in Figure 12, all corners of the mask patterns have a round shape. A round profile decreases errors and defects both in exposure and in latter processing steps, such as etching.

In the beginning, sample pieces of different III–V solar cell materials were cleaved with an automatic scriber (Dynatex International). An ohmic back contact with the structure of Ti/Pt/Au with respective layer thicknesses of 50/50/200 nm was deposited on the back side of the samples with an e-beam metal evaporator (Instrumentti Mattila). Prior to metal deposition, native oxides were removed by an ammonia (Honeywell Specialty Chemicals Seelze GmbH) based solution. Then, the front contact grid was fabricated following the steps of the photolithographic process flow presented in Figure 11. At first, the protective SiO_2-layer was deposited onto the front surfaces of samples by plasma-enhanced chemical vapor deposition. Then, a negative AZ nLof 2035 photoresist (AZ Electronic Materials GmbH) was deposited on the samples using an automatic OPTIcoat ST23+ spinner (ATMsse). The coated samples were exposed with UV light with the Karl Süss Mask Aligner. The grid pattern was opened by removing unexposed areas of the photoresist with AZ 726 MIF and AZ 826 MIF developers (AZ Electronic Materials GmbH). Prior to metal evaporation, the SiO_2-layer was etched from the photoresist openings by buffered hydrogen fluoride (Honeywell Specialty Chemicals Seelze GmbH) and native oxides were removed. The front contacts with the structure of Ni/Au with respective layer thicknesses of 10/1500 nm were deposited by the e-beam evaporator. Subsequent to the evaporation, the excessive metal layer and the underlying photoresist was removed by a lift-off process utilizing the TechniStrip® NI555 photoresist stripper (Technic, Inc,). The quality of the front contact grid was investigated, and the contact finger widths were

measured with an optical microscope (Nikon). The contact fingers with their measured widths are shown in Figure 13.

Figure 13.   *An image of contact fingers taken with the optical microscope with the magnification of 50×.*

It was observed that the fingers were wider than what had been defined by the photomask for the photolithography (2.00 μm). This is a typical phenomenon in photolithography since received light intensity varies as a function of the depth in the photoresist layer [53]. Thus, the bottom layer of the negative photoresist receives less light than the topmost layer. As a result, part of the bottom layer gets less cross-linked and remains soluble in the developer. This leads to a negative sidewall profile in the photoresist openings where the openings are wider at the bottom than on the top.

After the fabrication of the front contacts, the mesa structures were first defined by a photolithographic process followed by etching of structures with inductively coupled plasma etching using BCl_3 and Ar based plasma. The purpose of mesa etching is to electrically isolate the device terminals of the solar cell and to produce high-quality sidewalls for the mesa to avoid parasitic losses and leakage current via sidewall. The final step of the solar cell process was the deposition of ARC on the front side of the solar cells. First, the photoresist mask was prepared to cover the busbar areas. Then, ARC with the structure of TiO_2/SiO_2 was deposited by e-beam evaporation. The fabricated solar cell component is presented in Figure 14.
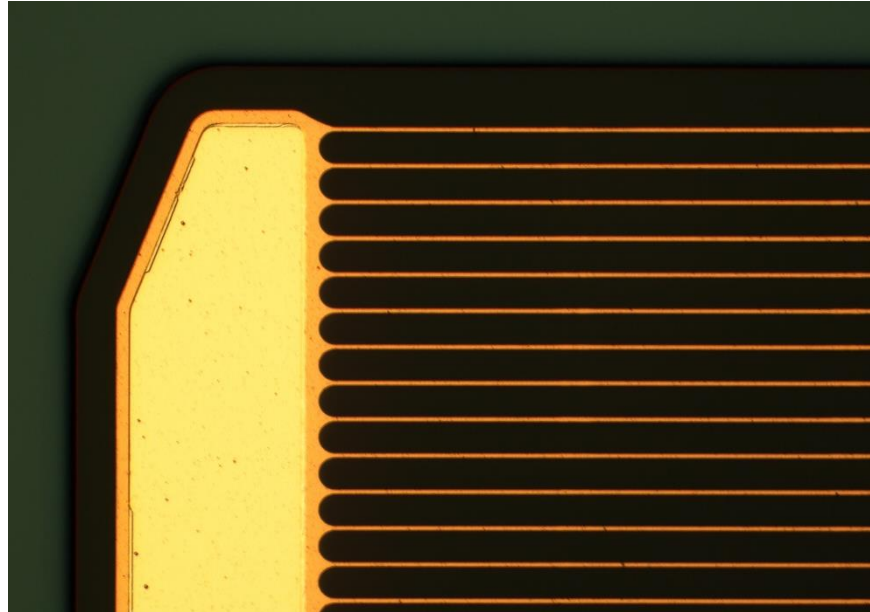
Figure 14.   *An optical microscope image of the front side of the fabricated solar cell with the magnification of 20×.*

Finally, individual solar cell chips were cleaved apart from the sample pieces and bonded on AlN submounts serving as heat sinks. Electrical contacts onto the submount were established by a conductive solder paste for the back contact and by wire-bonding with Au-wires for the front contact. As shown in Figure 14, ARC is removed from the busbar to enable the wire-bonding. On the submount, the front and the back contacts are electrically isolated. The finished and bonded solar cell component is presented in Figure 15.

4.2 One-sun and concentrated current-voltage measurements

The electrical behaviour of the fabricated solar cells was characterized by one-sun and concentrated IV measurements under AM1.5D (1000 W/m^2) standard spectra with a 7 kW TriSol solar simulator (OAI). The measurement principle of the solar simulator is to measure current produced by the solar cell at a certain voltage-range under illuminated and dark conditions. Investigated parameters retrieved from the IV measurements were η, FF, V_{OC}, J_{SC}, and P_m.

The electrical characterization was focused on the single-junction top cell of a multijunction solar cell, since it is assumed that the IV characteristics of the top cell are mostly influenced by the properties of the front contact. The key property of the top cell is to act as a lateral current spreading layer [58] which is illustrated in Figure 10. The measurement setup for one-sun conditions is presented in Figure 15, and for concentrated conditions in Figure 16, respectively. In CPV measurements, the investigated solar cell component was measured with values of the concentrator factor of approximately 200×,

400×, 600×, 800×, and 1000×. The solar simulator works on a steady-state domain so that the heating of the solar cells during the measurements cannot be fully avoided. Typically, CPV devices are measured with a flash light illumination for a few milliseconds [22], whereas the measurements conducted in this work take roughly 0.3 seconds.
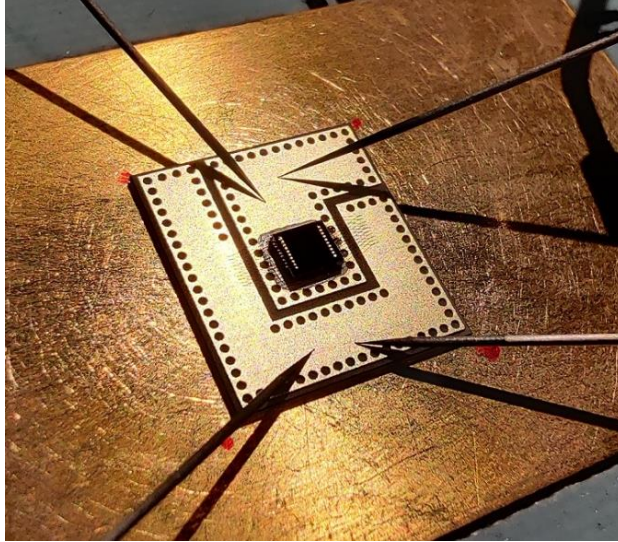
Figure 15. *The four-probe measurement setup for one-sun conditions.*
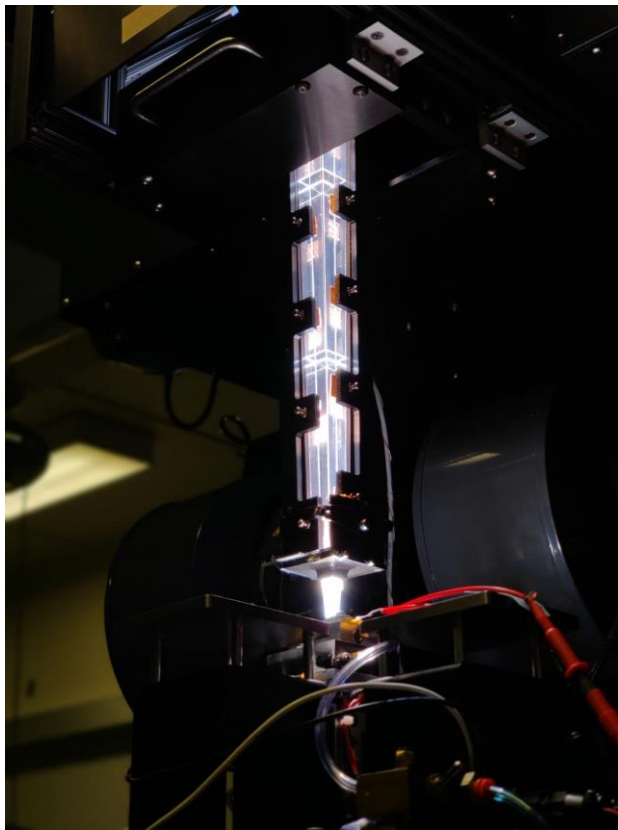
***Figure 16.*** *The measurement setup for concentrated conditions.*

4.3 Simulation model

The simulation model used in this thesis work is based on MathWorks MATLAB and Simulink tools and has been developed in previous thesis works [59, 60]. The model uses the solar cell block from the Simulink library Simscape/Electrical/Sources in which the solar cell is modelled as an electrical circuit with a current source in parallel with a diode and a parallel resistor which are connected in series with a series resistor. The model for the solar cell is calculated according to parameters retrieved from real measurements. [61] The parameters utilized in the modelling were I_{SC}, V_{OC}, R_S, n, and the power density of the simulated solar radiation. The model also allows for the calculation of temperature-dependence for different parameters. Temperature-coefficients can also be retrieved from real measurements for the model. [60] Once a sufficient model for the investigated solar cell component was calculated, the model was utilized to investigate the optimal design for the front contact. The performance of the solar cell under concentrated conditions was calculated with different dimensions and structures of the front contact.

5. RESULTS AND ANALYSIS

In this chapter, the results from the IV measurements as well as observations and conclusions based on the results are presented. Moreover, simulated results for the further investigation of the optimal properties for the front contact grid are presented and discussed.

5.1 Current-voltage measurements

First, the IV characteristics of the fabricated solar cells with different contact finger spacings were measured under one-sun conditions. The IV curves for all finger spacings are shown in Figure 17. In this, the values of current are normalized to the value of I_{SC} of the solar cell component with the finger spacing of 125 µm under chosen measurement conditions. The same normalization is also applied to the results presented in Figure 18.
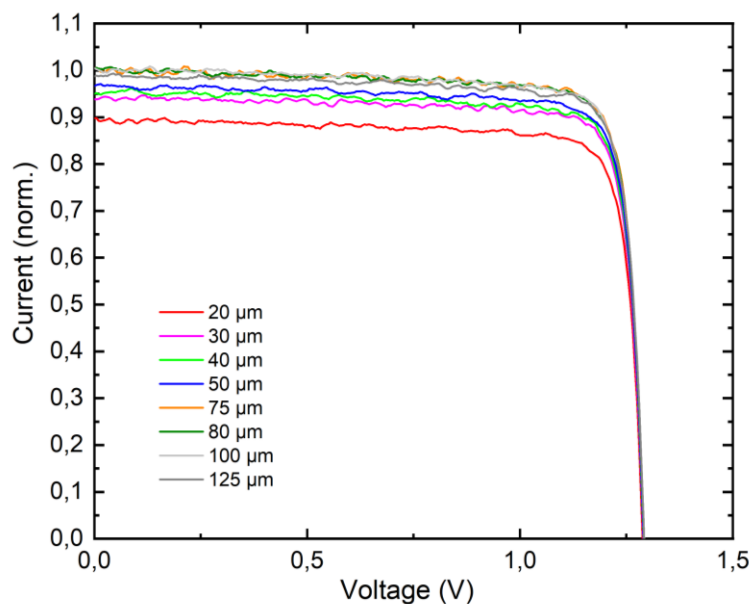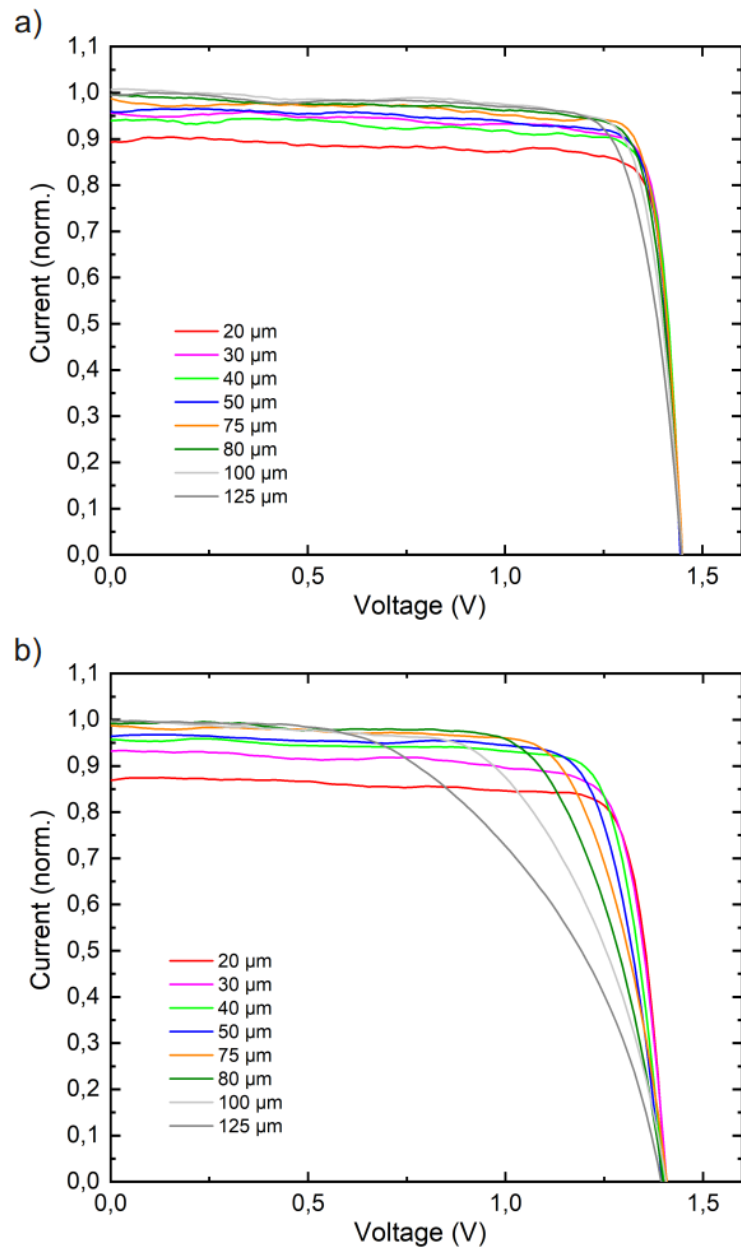

Figure 17.   *The IV curve for each finger spacing at one-sun conditions.*

The IV characteristics for all the solar cells with different finger spacings show good electrical behaviour which can be assumed by the shape of the IV curves. It indicates that the values of *FF* remain consistent with all the finger spacings as well as that there is barely any undesirable leakage current from the solar cells. In addition, values of V_{OC} remain almost constant for all finger spacings which agrees well with the theory stating that the value of V_{OC} is more of a measure of recombination of charge carriers rather than an illumination-dependent parameter because of the logarithmic dependence on I_{SC}

shown in Equation 6 [6]. On the other hand, the finger spacing is clearly affecting the values of I_{SC} since these values increase as the shadowing effect of the front contact decreases.

Subsequent to one-sun measurements, the IV characteristics were measured under concentrated conditions for the solar cells and the results are presented in Figure 18. Here, only the measurement results at 200× and 1000× are shown to compare the electrical behaviour of the solar cells under low and high concentrated conditions. The measured IV characteristics at 400×, 600×, and 800× are presented in Appendix A.

**Figure 18.** *The IV curve for each finger spacing at a concentration of a) 200× and b) 1000×.*

The IV characteristics show similar electrical behaviour at the concentration of 200× as under one-sun conditions which proves that resistive effects are still insignificant at low concentrations for the measured solar cells. The only exception is the solar cell with the finger spacing of 125 µm which shows the rapid drop of current at a slightly lower value of voltage than for the other finger spacings. It is seen that resistive losses are starting to dominate the electrical behaviour of the solar cell with the 125 µm finger spacing at the concentration of 200×. Moreover, resistive effects are clearly shown from the shape of the IV curves at the concentration of 1000× with the increasing finger spacing.

An another noticeable effect shown in the IV curves in Figure 18 is the drop of the values of V_{OC} when the value of the concentration factor is increased from 200 to 1000. Because of the steady-state measurement approach, it can be assumed that the heating of the solar cells cancels out the increase of V_{OC} with the concentration factor. The dependency of V_{OC} on temperature with the value of -2.5 mV/°C has been determined to the solar cell with a structure corresponding to the ones investigated in this work [23]. Therefore, an effective cooling of the solar cell is needed for the optimal performance when the solar cells are operated under high concentration.

5.1.1 Optimal finger spacing

The results from the IV measurements show that the finger spacing significantly affects the overall electrical performance of the solar cells when the concentration level is increased from 200× to 1000×. In addition, it is observed that the measured results agree well with the theory stating that the shadowing is the main power loss mechanism under one-sun conditions, whereas the resistive effects become dominant when a high concentration level is used. To further examine the effect of the finger spacing on the electrical behaviour of the solar cell, the values of η can be determined for each finger spacing at the measured conditions. Moreover, the values of FF should be considered to further examine the resistive effects. The values of η and FF are retrieved from the IV measurements. The results are shown in Figure 19. The values of V_{OC}, J_{SC}, and P_m for each finger spacing at the measured conditions are presented in Appendix B. In addition, the comparison of the simulated and the measured results for η are presented in Figure 20. In this, the simulated values are presented with a dashed line and the measured values as data points.

a)

b)
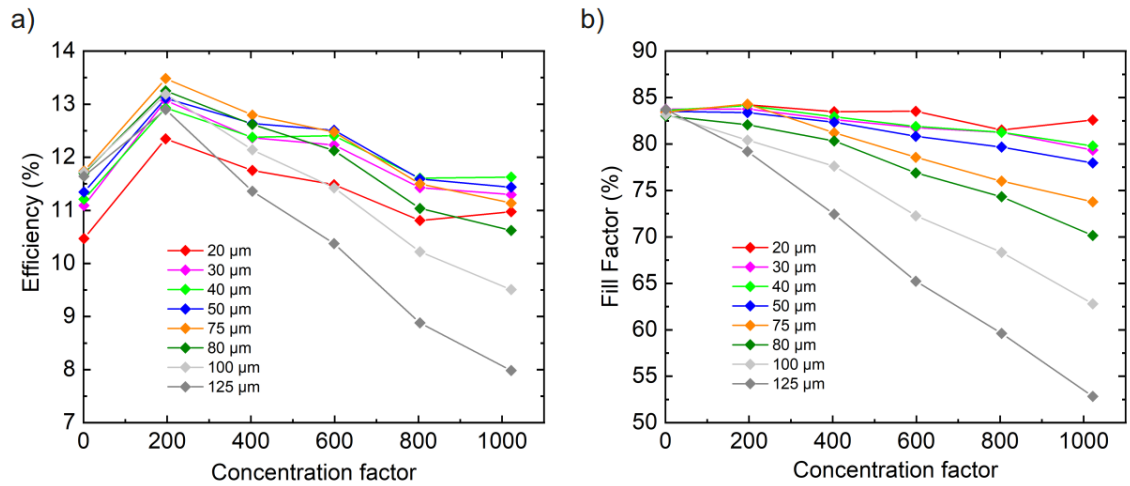
Figure 19. *a) Efficiency and b) fill factor as a function of concentration factor for each finger spacing.*

The measured single-junction solar cell gives the highest value of η at the concentration of 200× with the finger spacing of 75 µm. However, as the concentration level is increased, it is noticed that the finger spacing giving the highest value of η decreases. Thus, the maximum value of η at the concentration of 1000× is measured with the finger spacing of 40 µm. The overall drop in the values of η can be explained by the increased temperature of the solar cells under higher levels of concentration. There is also a clear decrease in *FF*, especially, with the finger spacings of 75 µm, 80 µm, 100 µm, 125 µm as the concentration level increases which can be explained by considerable resistive losses. On the other hand, the value of *FF* for the finger spacing of 20 µm remains almost constant when the concentration level is increased.
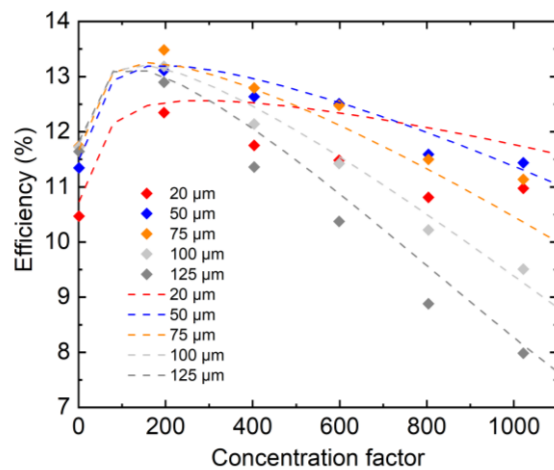

Figure 20. *Simulated and measured efficiency as a function of concentration factor.*

The use of the simulation model was validated by comparing the simulated and measured results. It is shown that the simulated values obey the trend of the measured values

only with small deviations. The most considerable difference in the simulated and the measured results is for the finger spacing of 20 µm at the concentration levels above 200×. As shown in the IV measurements, I_{SC} of the solar cell with the finger spacing of 20 µm is clearly lower than for other finger spacings which could, for example, result from the processing.

It can be concluded from the measurements that the finger spacing should be reduced to compensate the resistive power losses when the concentration level is increased. Thus, the optimal finger spacing can be determined for different levels of concentration. Figure 21 presents the optimal finger spacing for the fabricated solar cells as well as the obtained maximum value of η at each concentration level that was used in the IV measurements. The exact values of η and the finger spacing are listed in Table 1. The concentration level with the value of 1 represents the one-sun conditions.
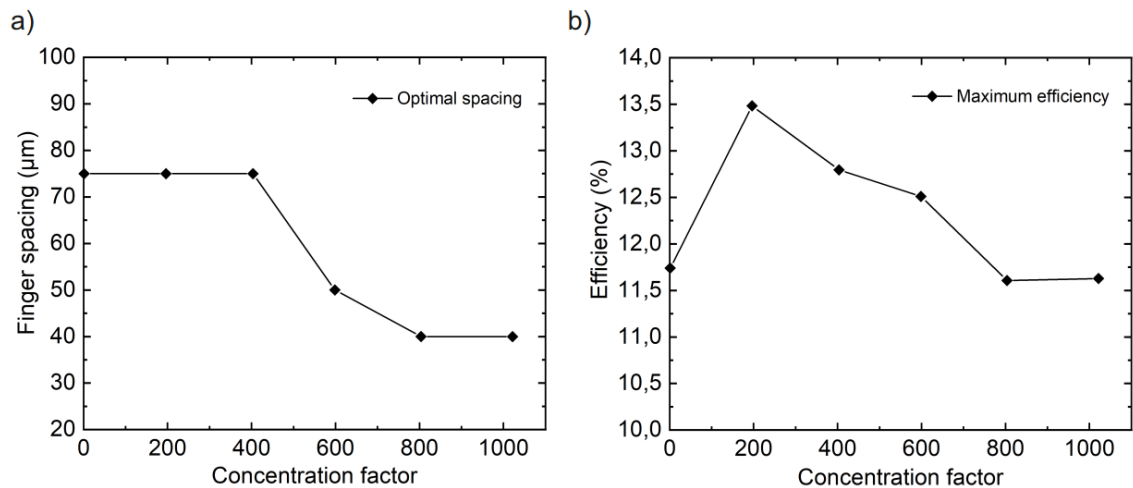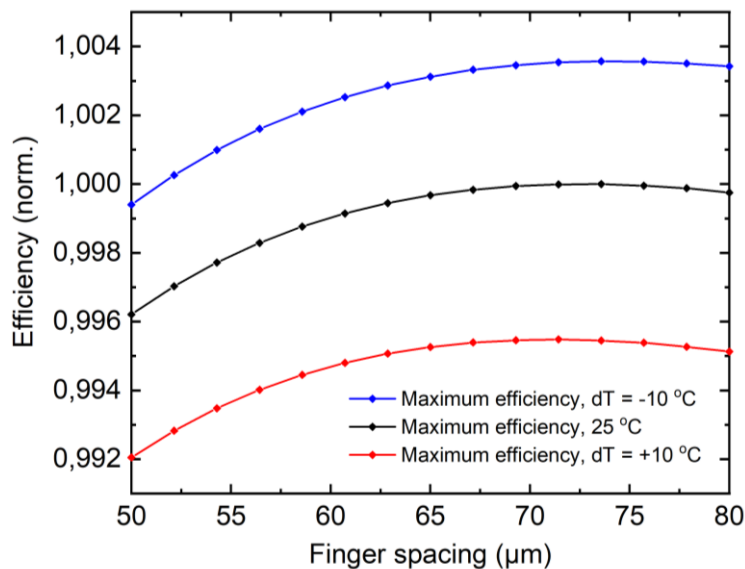

Figure 21. a) The finger spacing giving the highest measured efficiency, and b) the maximum efficiency at each concentration level.

Table 1. The measured maximum value of η with the optimal finger spacing at each concentration level.

Concentration level	Finger spacing (µm)	η (%)
1	75	11.74
200	75	13.48
400	75	12.80
600	50	12.51
800	40	11.61
1000	40	11.63

5.1.2 Temperature analysis

To estimate the effect of temperature increase on to the measured results, the simulation tool was used to calculate η as a function of the finger spacing with temperature of the solar cell initially set to 15°C, 25°C, and 35°C under one-sun conditions from where it rises with an increasing concentration level. Based on the previous experiments, the real temperature of the solar cell in the IV measurements is assumed to remain at the range defined in the simulations. The calculated dependency of η on temperature and the finger spacing is shown in Figure 22. In the simulations, the width of the contact finger was set to 2.3 µm and the height to 1.5 µm which correspond to the measured values for the fabricated front contacts. The values of η are normalized to the maximum value at 25°C. In addition, the level of concentration was considered in the simulations. The concentration level giving the highest η was used and it varied between each data point. Overall, the value of the concentration factor varied approximately from 150 to 200.
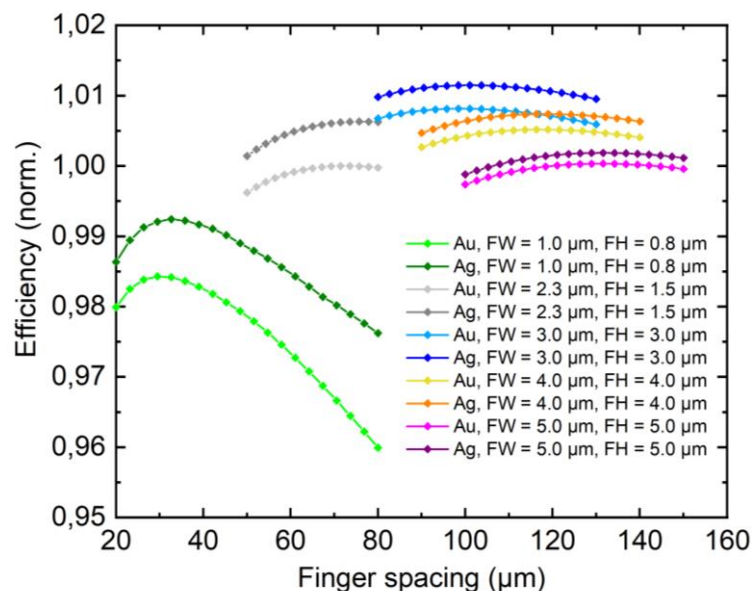

Figure 22.   *The simulated efficiency as a function finger spacing at different temperatures.*

It is shown that the finger spacing giving the maximum η is close to 75 µm which agrees well with the measured results. According to the simulations, the optimal finger spacing for the solar cell varies between 71,43 µm and 73,57 µm due to temperature change. Thus, increase of temperature would reduce the optimal finger spacing only slightly. The effect of temperature variation on the values of η is also clearly shown which gives rise to the need of an effective cooling system for the measurement setup.

5.2 Properties of the front contact

Furthermore, the simulation tool validated by the measurements was utilized to calculate the optimal finger spacing with different properties of the front contact. The contact finger width (FW) was varied from 1.0 µm to 5.0 µm and the height (FH) from 0.8 µm to 5.0 µm. In addition, all dimensions were considered for the front contact made of Au and Ag. The results are presented in Figure 23. In these simulations, the concentration level was also considered. The level of concentration varied between all the data points and the overall variation was approximately from 85× to 230×. The values of η were normalized to the maximum value of η obtained with the front contact made of Au and with the value of FW as 2.3 µm and FH as 1.5 µm which correspond to the properties of the fabricated front contacts.

Figure 23. *Simulated results for efficiency as a function of finger spacing for Au and Ag contact fingers with varying dimensions.*

It can be observed from the simulated results that the front contact made of Ag would give a higher value of η with all the dimensions considered. Especially, when the dimensions of the contact finger are reduced, it would be more beneficial to use Ag instead of Au which can be assumed to result from the better conductivity of Ag. It is also shown that the finger spacing with the reduced dimensions of the contact fingers must be chosen more carefully since the peak of the curve becomes sharper when compared to larger dimensions. Thus, it can also be assumed that the resistivity of the contact finger becomes the dominating source of power loss in the case of reduced dimensions of the contact fingers even though the finger spacing is reduced. However, the simulated re-

sults give only an estimation of the optimal properties since the cross-section of the contact fingers was assumed to be rectangular whereas the fabricated front contacts are wider at the bottom than on top which may affect, for example, the conductivity of the contact fingers.

In the simulated results, the highest value of η would be reached with the dimensions of the contact finger with FW set to 3.0 µm and FH set to 3.0 µm for the solar cell in question. However, the change of dimensions and how it affects the photolithographic fabrication process should be considered. For example, the thickness of the photoresist layer must exceed the height of the deposited metal layer to enable the lift-off process. In addition, the choice of photoresist as well as other aspects such as process parameters and equipment affect the attained pattern resolution [52]. Lastly, the thickness of the metal layer can affect the choice of the deposition technique because the deposition of relatively thick layers becomes time-consuming with certain techniques such as e-beam evaporation. In addition, in the case of noble metals, the high material costs need consideration.

6. CONCLUSIONS

III-V semiconductor solar cells under concentrated sunlight have achieved the highest power conversion efficiencies when compared to other solar cell technologies. In this thesis, the front contact design for III–V semiconductor solar cells under concentrated conditions with high intensity of solar radiation was studied and optimized. Resistive effects associated with the front contact are a significant source of power loss in high concentration photovoltaic applications where the used concentration level is typically increased up to 1000 suns.

In the experimental part of this work, the effect of the front contact design on the electrical performance of the solar cells was studied by fabricating solar cells with eight different contact finger spacings varying from 20 µm to 125 µm using photolithographic processing. The current-voltage measurements of the solar cells under varying concentrated conditions showed the predicted behaviour of the trade-off between the resistive and the shadowing losses as the concentration level was increased up to 1000 suns. By comparing the current-voltage characteristics under the concentration of 200 suns and 1000 suns, the optimal contact finger spacing giving the highest efficiency was reduced from 75 µm to 40 µm as the concentration level increased. The electrical characterization was focused on the single-junction top cell of a multijunction solar cell, that essentially acts as a lateral-current spreading layer, which resulted in the highest measured efficiency of 13.48% with the contact finger spacing of 75 µm under the concentration level of 200 suns. During the IV measurements, increase of temperature was observed to lower the values of V_{OC} when the concentration level was increased from 200 suns to 1000 suns. This cancelled the enhancement of efficiency with an increased concentration factor based on the theoretical assumptions. Thus, a more effective cooling system is required when the steady-state IV measurement setup is used.

The simulated current-voltage characteristics agreed well with the measured results, thus, the simulation model allowed for the further investigation of the optimal properties of the front contact. The comparison of Ag and Au showed the advantage of better conductivity of Ag, especially with reduced dimensions of the contact fingers. Moreover, the results showed a strong dependency of the optimal contact finger spacing on the dimensions of the front contact as well as used concentration level. Based on the obtained results, it can be concluded that the intended concentration level should be considered in advance of the fabrication of the solar cells since resistive losses can be significantly compensated with a carefully considered front contact design.

The experimental work on the optimization of the front contact design conducted in this thesis work is essential to the research on the multijunction solar cells with ultra-high efficiencies beyond 50%, as well as to advance the fabrication process of the solar cell devices. The further development of the photolithographic processing of the solar cells would allow for the fabrication of even more high-performing front contacts with optimized properties regarding the width, height, and spacing of the contact fingers. Moreover, the promising results from the simulations associated with the front contact made of Ag encourage to develop the fabrication process of the solar cells suitable for the Ag-based front contacts.

REFERENCES

[1] A. Jäger-Waldau, PV Status Report 2019, *Publications Office of the European Union*, 2020.

[2] Jäger-Waldau A, Kougias I, Taylor N, Thiel C. How photovoltaics can contribute to GHG emission reductions of 55% in the EU by 2030, *Renewable and Sustainable Energy Reviews*, vol. 126, pp. 109836, 2020.

[3] Streetman BG. Solid state electronic devices. 4th ed. Englewood Cliffs (N.J.): Prentice-Hall, 1995.

[4] Tiedje T, Yablonovitch E, Cody GD, Brooks BG. Limiting efficiency of silicon solar cells, *IEEE Transactions on Electron Devices*, vol. 31, pp. 711-716, 1984.

[5] Hegedus S, Luque A. Achievements and Challenges of Solar Electricity from Photovoltaics, Handbook of Photovoltaic Science and Engineering, Ed. by A. Luque and S. Hegedus. John Wiley & Sons, 2010.

[6] Gray JL. The Physics of the Solar Cell, Handbook of Photovoltaic Science and Engineering, Ed. by A. Luque and S. Hegedus. John Wiley & Sons, 2010.

[7] Shockley W, Queisser HJ. Detailed Balance Limit of Efficiency of p-n Junction Solar Cells, *Journal of Applied Physics*, vol. 32, pp. 510-519, 1961.

[8] Green M, Dunlop E, Hohl-Ebinger J, Yoshita M, Kopidakis N, Hao X. Solar cell efficiency tables (version 57), *Progress in Photovoltaics: Research and Applications*, vol. 29, pp. 3-15, 2021.

[9] Friedman DJ, Olson JM, Kurtz S. High-Efficiency III–V Multijunction Solar Cells, Handbook of Photovoltaic Science and Engineering, Ed. by A. Luque and S. Hegedus. John Wiley & Sons, 2010.

[10] Aho A, Isoaho R, Raappana M, Aho T, Polojärvi V, Tukiainen A, et al. Performance Study of Lattice-Matched Multijunction Solar Cells Incorporating GaInNAsSb Junctions with 0.7 - 1.4 eV Bandgap, *IEEE 46th Photovoltaic Specialists Conference (PVSC)*, 2019.

[11] Wiesenfahrt M, Philipps DSP, Bett DAW, Horowitz K, Kurtz DS. Study: Current Status of Concentrator Photovoltaic (CPV) Technology, *Fraunhofer Institute for Solar Energy Systems ISE*, 2017.

[12] Algora C, Rey-Stolle I. Handbook of Concentrator Photovoltaic Technology. New York: John Wiley & Sons, Incorporated, 2016.

[13] Algora C, Díaz V. Influence of series resistance on guidelines for manufacture of concentrator p-on-n GaAs solar cells, *Progress in Photovoltaics: Research and Applications*, vol. 8, pp. 211-225, 2000.

[14] The National Renewable Energy Laboratory. 2000 ASTM Standard Extraterrestrial Spectrum Reference E-490-00. Available: https://www.nrel.gov/grid/solar-resource/spectra-astm-e490.html (accessed April 14, 2021).

[15] Gueymard CA. Solar Radiation Spectrum, Solar Energy, Ed. by C. Richter, D. Lincot and C. A. Gueymard. New York, NY: Springer New York, 2013.

[16] ASTM International. ASTM G173-03(2020) Standard Tables for Reference Solar Spectral Irradiances: Direct Normal and Hemispherical on 37° Tilted Surface. Available: http://www.astm.org/cgi-bin/resolver.cgi?G173-03(2020) (accessed April 14, 2021).

[17] ASTM International. ASTM E490-00a(2019) Standard Solar Constant and Zero Air Mass Solar Spectral Irradiance Tables. Available: http://www.astm.org/cgi-bin/resolver.cgi?E490-00a(2019) (accessed April 14, 2021).

[18] Hecht E. Optics. 4th ed. San Francisco: Addison Wesley, 2002.

[19] M. Brozel. Gallium Arsenide, Springer Handbook of Electronic and Photonic Materials, S. Kasap and P. Capper. Springer US, 2007.

[20] Kalogirou S. McEvoy's Handbook of Photovoltaics: Fundamentals and Applications. San Diego: Elsevier Science & Technology, 2017.

[21] Cotal H, Fetzer C, Boisvert J, Kinsey G, King R, Hebert P, et al. III–V multijunction solar cells for concentrating photovoltaics, *Energy & Environmental Science*, vol. 2, pp. 174-192, 2009.

[22] Wiesenfarth M, Anton I, Bett AW. Challenges in the design of concentrator photovoltaic (CPV) modules to achieve highest efficiencies, *Applied Physics Reviews*, vol. 5, pp. 041601, 2018.

[23] Aho A, Isoaho R, Tukiainen A, Polojärvi V, Aho T, Raappana M, et al. Temperature coefficients for GaInP/GaAs/GaInNAsSb solar cells, *AIP Conference Proceedings*, vol. 1679, pp. 050001, 2015.

[24] Friedman DJ. Progress and challenges for next-generation high-efficiency multijunction solar cells, *Current Opinion in Solid State and Materials Science*, vol. 14, pp. 131-138, 2010.

[25] Colter P, Hagar B, Bedair S. Tunnel junctions for III-V multijunction solar cells review, *Crystals*, vol. 8, 2018.

[26] Singh J. Electronic and optoelectronic properties of semiconductor structures. Cambridge; Cambridge University Press, 2003.

[27] Henini M, editor. Molecular Beam Epitaxy: From Research to Mass Production. Saint Louis: Elsevier Science & Technology, 2012.

[28] Danilchenko B, Budnyk A, Shpinar L, Poplavskyy D, Zelensky SE, Barnham KWJ, et al. 1MeV electron irradiation influence on GaAs solar cell performance, *Solar Energy Materials and Solar Cells*, vol. 92, pp. 1336-1340, 2008.

[29] Gruginskie N, Cappelluti F, Bauhuis GJ, Mulder P, Haverkamp EJ, Vlieg E, et al. Electron radiation–induced degradation of GaAs solar cells with different architectures, *Progress in Photovoltaics: Research and Applications*, vol. 28, pp. 266-278, 2020.

[30] The National Renewable Energy Laboratory. Photovoltaic Research: Best Research Cell Efficiency Chart. Available: https://www.nrel.gov/pv/cell-efficiency.html (accessed February 20, 2021).

[31] Hong H-F, Huang T-S, Chen Y-Y. Influence of metal grid spacing on the conversion efficiency of concentration solar cell at different illumination levels, *Materials Science and Engineering: B*, vol. 188, pp. 43-47, 2014.

[32] Wen L, Yueqiang L, Jianjun C, Yanling C, Xiaodong W, Fuhua Y. Optimization of grid design for solar cells, *Journal of Semiconductors*, vol. 31, pp. 014006, 2010.

[33] Ward JS, Duda A, Friedman DJ, Geisz J, McMahon W, Young M. High aspect ratio electrodeposited Ni/Au contacts for GaAs-based III–V concentrator solar cells, *Progress in Photovoltaics: Research and Applications*, vol. 23, pp. 646-653, 2015.

[34] Huo P, Rey-Stolle I. Al-based front contacts for HCPV solar cell, *AIP Conference Proceedings*, vol. 1881, pp. 040004, 2017.

[35] Cavalli A, Buencuerpo J, Steger M, Perl EE, Steiner M, Geisz J. Development of Solar Cells with Trapezoidal Grid Fingers, *IEEE 46th Photovoltaic Specialists Conference (PVSC)*, 2019.

[36] Salmi J. Metalloinnin erikoiskysymyksiä, Tampere University of Technology, 2014.

[37] Baca AG, Ashby CIH. Fabrication of GaAs devices. London: Institution of Electrical Engineers, 2005.

[38] Raappana M, Aho A, Aho T, Isoaho R, Anttola E, Kajas N, et al. Performance of Solar Cell Grids based on Ag, Au, and Al for Cost-Effective Manufacturing, *European Space Power Conference (ESPC)*, pp. 1-3, 2019.

[39] Chen H-L, Cattoni A, De Lépinau R, Walker AW, Höhn O, Lackner D, et al. A 19.9%-efficient ultrathin solar cell based on a 205-nm-thick GaAs absorber and a silver nanostructured back mirror, *Nature Energy*, vol. 4, pp. 761-767, 2019.

[40] Fei Guo C, Sun T, Cao F, Liu Q, Ren Z. Metallic nanostructures for light trapping in energy-harvesting devices, *Light: Science & Applications*, vol. 3, pp. e161, 2014.

[41] Mellor A, Hylton NP, Hauser H, Thomas T, Lee K, Al-Saleh Y, et al. Nanoparticle Scattering for Multijunction Solar Cells: The Tradeoff Between Absorption Enhancement and Transmission Loss, *IEEE Journal of Photovoltaics*, vol. 6, pp. 1678-1687, 2016.

[42] Aho T. Advanced III-V Solar Cells with Back Reflectors, Tampere University, 2020.

[43] Nakayama K, Tanabe K, Atwater HA. Plasmonic nanoparticle enhanced light absorption in GaAs solar cells, *Applied Physics Letters*, vol. 93, pp. 121904, 2008.

[44] Li K, Haque S, Martins A, Fortunato E, Martins R, Mendes MJ, et al. Light trapping in solar cells: simple design rules to maximize absorption, *Optica*, vol. 7, pp. 1377-1384, 2020.

[45] Chong TK, et al. Optimal wavelength scale diffraction gratings for light trapping in solar cells, *Journal of Optics*, vol. 14, pp. 024012, 2012.

[46] Massiot I, Vandamme N, Bardou N, Dupuis C, Lemaître A, Guillemoles J-F, et al. Metal Nanogrid for Broadband Multiresonant Light-Harvesting in Ultrathin GaAs Layers, *ACS Photonics*, vol. 1, pp. 878-884, 2014.

[47] van de Groep J, Spinelli P, Polman A. Transparent Conducting Silver Nanowire Networks, *Nano Letters*, vol. 12, pp. 3138-3144, 2012.

[48] Catchpole KR, Mokkapati S, Beck F, Wang E-C, McKinley A, Basch A, et al. Plasmonics and nanophotonics for photovoltaics, *MRS Bulletin*, vol. 36, pp. 461-467, 2011.

[49] Saive R, Borsuk AM, Emmer HS, Bukowsky CR, Lloyd JV, Yalamanchili S, et al. Effectively Transparent Front Contacts for Optoelectronic Devices, *Advanced Optical Materials*, vol. 4, pp. 1470-1474, 2016.

[50] Huo P, Lombardero I, García I, Rey-Stolle I. Enhanced performance of GaInP/GaAs/Ge solar cells under high concentration through Pd/Ge/Ti/Pd/Al grid metallization, *Progress in Photovoltaics: Research and Applications*, vol. 27, pp. 789-797, 2019.

[51] Lithography, Ed. by Stefan Landis John Wiley & Sons, Incorporated, 2010.

[52] Microchemicals GmbH. Photoresists. Available: https://www.microchemicals.com/products/photoresists.html (accessed March 2, 2021).

[53] Levinson HJ. Principles of Lithography, Fourth Edition. Bellingham: Society of Photo-Optical Instrumentation Engineers, 2019.

[54] Tallents G, Wagenaars E, Pert G. Optical lithography: Lithography at EUV wavelengths, *Nature Photonics*, vol. 4, pp. 809-811, 2010.

[55] Massiot I, Colin C, Péré-Laperne N, Roca i Cabarrocas P, Sauvan C, Lalanne P, et al. Nanopatterned front contact for broadband absorption in ultra-thin amorphous silicon solar cells, *Applied Physics Letters*, vol. 101, pp. 163901, 2012.

[56] Hsu P-C, Wang S, Wu H, Narasimhan VK, Kong D, Ryoung Lee H, et al. Performance enhancement of metal nanowire transparent conducting electrodes by mesoscale metal wires, *Nature Communications*, vol. 4, pp. 2522, 2013.

[57] Guo LJ. Nanoimprint Lithography: Methods and Material Requirements, *Advanced Materials*, vol. 19, pp. 495-513, 2007.

[58] Ochoa M, Barrigón E, Barrutia L, García I, Rey-Stolle I, Algora C. Limiting factors on the semiconductor structure of III–V multijunction solar cells for ultra-high concentration (1000–5000 suns), *Progress in Photovoltaics: Research and Applications*, vol. 24, pp. 1332-1345, 2016.

[59] Hyötylä E. Keskitetyn auringonvalon moniliitosaurinkokennojen kytkentöjen mallintaminen ja tehon optimointi aurinkopaneelissa, Tampere University of Technology, 2018.
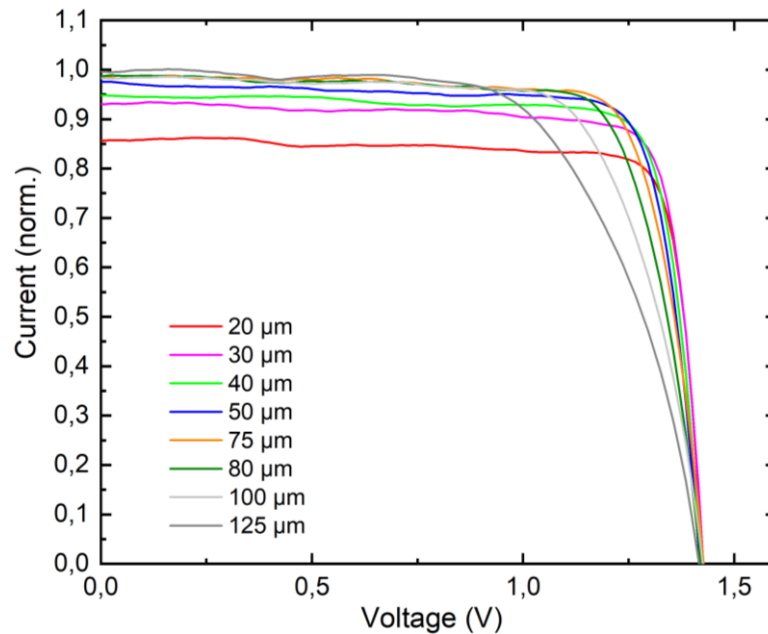
[60] Peltomaa L. Moniliitoskennorakenteen optimointi Simulink-mallinnuksella, Tampere University, 2020.

[61] Mathworks. Solar Cell Documentation. Available: https://se.mathworks.com/help/physmod/sps/ref/solarcell.html (accessed April 28, 2021).
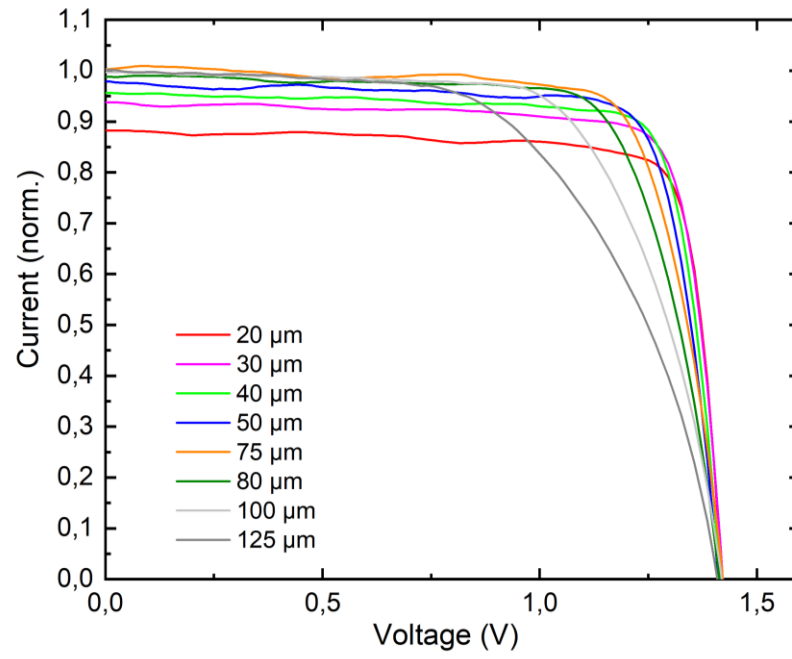
APPENDIX A: CURRENT-VOLTAGE CHARACTERISTICS
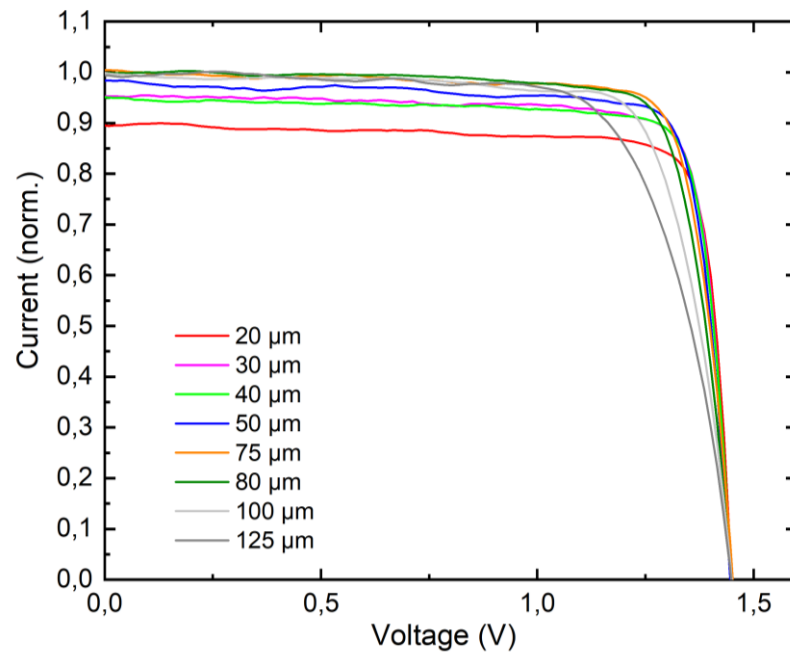
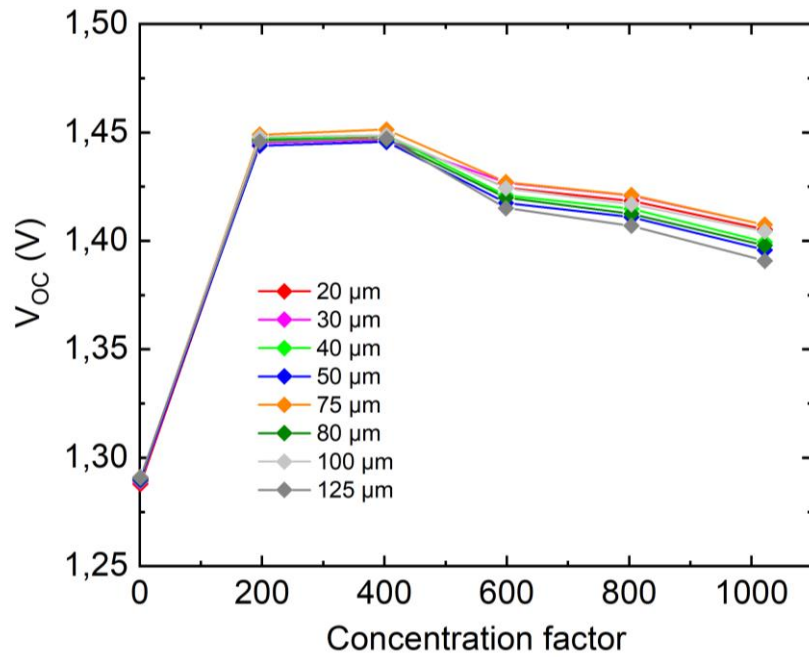*Figure 24.*   *The IV curve for each finger spacing at a concentration of 400×.*

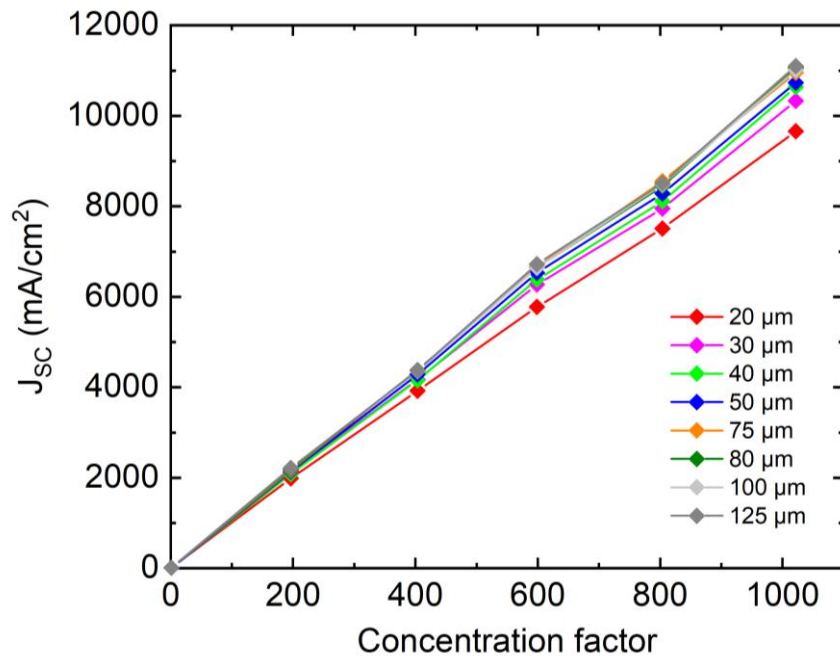*Figure 25.*   *The IV curve for each finger spacing at a concentration of 600×.*

Figure 26. *The IV curve for each finger spacing at a concentration of 800×.*

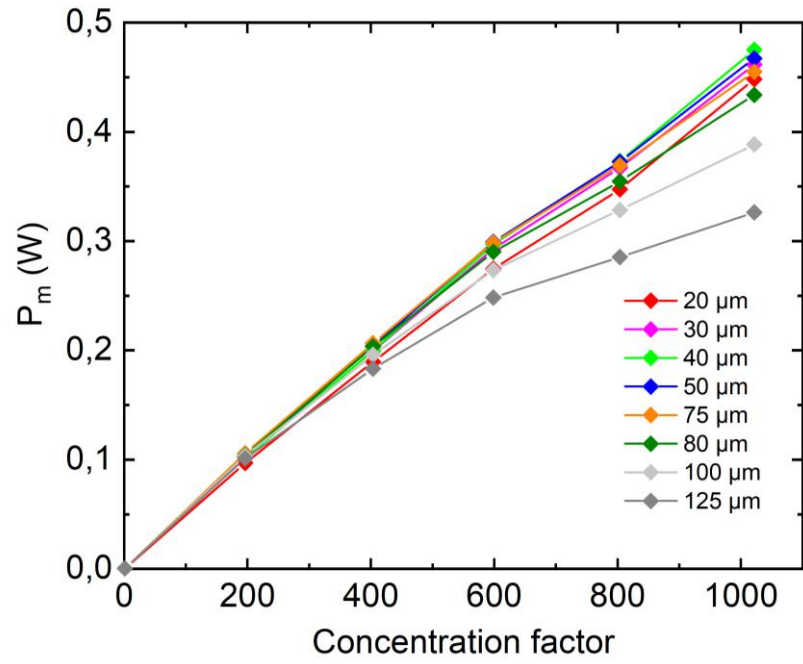# APPENDIX B: CHARACTERISTIC PARAMETERS

Figure 27. V_{OC} as a function of concentration factor for each finger spacing.

Figure 28. J_{SC} as a function of concentration factor for each finger spacing.

Figure 29. *P_m as a function of concentration factor for each finger spacing.*